

Review of point defect structures in hexagonal close packed metals and across the Periodic Table

Andrew R. Warwick, Pui-Wai Ma, and Sergei L. Dudarev
 UK Atomic Energy Authority, Culham Science Centre, Oxfordshire, OX14 3DB, United Kingdom
 (Dated: May 26, 2025)

We present a comprehensive *ab initio* dataset of formation energies and elastic properties of intrinsic point defects across all the transition and rare earth hexagonal close packed (hcp) metals, as well as metalloid elements with hcp crystal structure. Point defect properties appear weakly correlated with the c/a ratio of the hcp lattice. Instead, it is the position of an element in the Periodic Table that primarily defines the relaxation volume tensor, elastic dipole tensor and formation energy of a point defect. This suggests that the local variations in the electronic structure and interatomic bonding at the core of a defect dominate its properties, as opposed to long-range elastic deformations. Across all the metals, we find that the relaxation volumes of vacancies and self-interstitial defects are correlated with atomic volumes, with values of -0.35 and 1.46 atomic volumes for a vacancy and a self-interstitial defect, respectively, providing a universally good approximation independent of the crystal structure. This study complements and completes the existing point defect databases spanning body-centred cubic and face-centred cubic metals.

I. INTRODUCTION

Properties of metals are sensitive to perturbations of their underlying crystal structure. Intrinsic point defects are the simplest types of lattice defects, involving the removal or insertion of a single atom. Vacancies and self-interstitial atom (SIA) defects are readily created, for example, by high-energy particle irradiation in a nuclear reactor. Their coalescence into larger, extended defects, such as dislocations and voids, is among the causes of hardening and embrittlement. The accumulation of point defects also gives rise to dimensional changes and swelling.

Defects interact through long-range elastic fields, with the strength of interaction determined by elastic dipole tensors P_{ij} [1, p. 161]. A sample of the host metal, free from body forces and tractions, changes shape and volume according to the relaxation volume tensor $\Omega_{ij} = S_{ijkl}P_{kl}$ [2, 3] of the defects contained in it, where S_{ijkl} is the elastic compliance tensor [4, p. 29]. Models for microstructural evolution at larger length scales, treating interactions between the defects, require these tensorial quantities as input. Compiling a database of point defect elastic tensors is a necessary step involved in predicting deformations of materials operating in an irradiation environment.

P_{ij} and Ω_{ij} for a vacancy and various SIA configurations have been computed *ab initio* and tabulated across all the body centred cubic (bcc) [2] and face centred cubic (fcc) [3] metals, save the lanthanides and actinides. The lowest energy SIA structure in all the bcc metals has the $\langle 111 \rangle$ symmetry, bar magnetic Fe [5]. In Cr, Mo and W the $\langle 111 \rangle$ symmetry is slightly broken by the buckling occurring in the core of the defect [6, 7]. In fcc metals, the $\langle 100 \rangle$ dumbbell is often, but not always, the lowest energy SIA configuration.

A compilation of point-defect elastic dipole and relaxation volume tensors for the hexagonal close-packed (hcp) metals is currently missing. Many hcp metals play

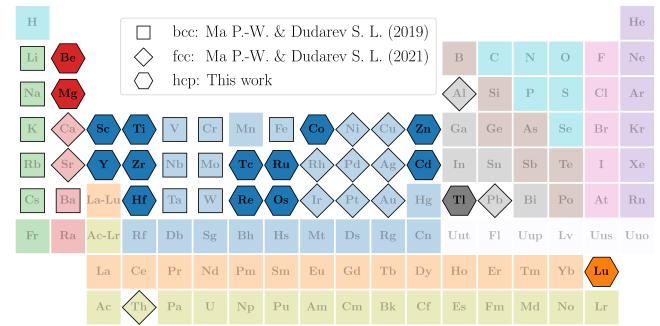


FIG. 1: The elements with hcp structure considered in this work and highlighted by hexagon cells. The bcc [2] and fcc [3] metals considered in previous studies are depicted by the bordered squares and diamonds, respectively. Most of the lanthanide and actinide hcp metals were not included in this study.

an important role in engineering applications such as lightweight structural components composed of Mg [8] or Ti [9], Zr nuclear fuel claddings [10], and Be as a candidate neutron multiplier material in nuclear fusion reactors [11].

Until now, Pasianot [12] has conducted the most comprehensive *ab initio* study of elastic properties of point defects in hcp metals. The trends in the defect formation energy, dipole tensors, and relaxation volumes with respect to the c/a ratio were explored and compared to resistivity recovery, internal friction, and Huang diffuse X-ray scattering (DXS) data. Seven elements were included in the study [12]: the two elements that have a larger than ideal c/a ratio, Cd and Zn, as well as Be, Ti, Zr, Mg and Co. For Be, Ti and Zr, the lowest formation energy SIA was found to be the basal octahedral (BO) configuration, with Mg and Co instead favouring the crowdion (C) and [0001] split dumbbell (S) defect structure, respectively. The SIA formation energies

computed for Cd and Zn showed a clear preference for the out-of-basal-plane configurations over the basal SIAs. Due to the ease of transformation of the ground state configuration of the defect into alternative configurations, it was suggested that SIA migration is likely to be three-dimensional in Zn, Cd and Mg. The predicted values of P_{ij} were compared with Huang diffuse X-ray scattering (DXS) measurements, suggesting that the computed and experimentally measured values were often not compatible with each other. Dipole tensor calculations have also been performed for the group IV hcp metals Ti, Zr and Hf [13], showing that in Zr the SIA configurations with monoclinic symmetry had the lowest energy and were consistent with internal friction experimental measurements. The elastic properties of defects across the Periodic Table have also been investigated using EAM potentials [14–16], which often exhibit relatively poor accuracy in comparison with *ab initio* calculations.

Most studies of defects in hcp metals focussed on formation and migration energies [17]. Of particular note are the *ab initio* high throughput calculations conducted by Shang *et al.* [18] that have yielded a complete database of energies for vacancy defects across *all* the elements in the Periodic Table, including the elements with hcp crystal structure. Self-interstitial atom defects have been investigated, using *ab initio* methods, in Zn [19], Be [20, 21], Y [22], Ti [13, 23–26], Zr [13, 27–38], Mg [39, 40], Dy [41], Hf [13] and Sc [42]. The results are broadly consistent with an earlier hypothesis that the SIAs lying in the basal plane are the most stable configurations in all the hcp elements with the lower than ideal c/a ratio [43].

In this study, we compute the formation energies, dipole tensors and relaxation volume tensors of all the hcp metals and hcp metalloid elements in the Periodic Table, with the exception of lanthanides and actinides, shown in Figure 1 by the hexagon symbols. The bcc [2, 7] and fcc [3] metals studied earlier are denoted by squares and diamonds, respectively. We outline the point defect configurations and simulation methods in section II, followed by the tabulation and analysis of our results in section III, with conclusions provided in section V.

II. METHODOLOGY

Density functional theory (DFT) calculations were performed using the *Vienna Ab-Initio Simulation Package* (VASP) version 6.4.1 [45–48]. In Table I we summarise the selected plane wave energy cut-off E_{cut} , k -point mesh and valence electron configuration of the plane augmented wave (PAW) pseudopotential [49, 50] for each hcp metal. For a given element, we have chosen the pseudopotential with the lowest number of core electrons, to achieve the highest possible accuracy in the treatment of interatomic interactions at short distances in the SIA structures. The results of convergence tests are given in the Supplementary Material. The energies computed by the self-consistent field method were converged to within 10^{-8} eV

Element	Valence electrons	E_{cut} (eV)	k -grid
Be	$1s^2 2s^2$	800	$19 \times 19 \times 12$
Mg	$2s^2 2p^6 3s^2$	1000	$17 \times 17 \times 11$
Sc	$3s^2 3p^6 4s^1 3d^2$	700	$11 \times 11 \times 07$
Y	$4s^2 4p^6 5s^1 4d^2$	400	$17 \times 17 \times 11$
Lu	$5s^2 5p^6 4f^{14} 6s^2 5d^1$	600	$13 \times 13 \times 08$
Ti	$3s^2 3p^6 4s^1 3d^3$	600	$15 \times 15 \times 09$
Zr	$4s^2 4p^6 5s^1 4d^3$	700	$17 \times 17 \times 11$
Hf	$5s^2 5p^6 5d^4$	700	$17 \times 17 \times 11$
Tc	$4p^6 4d^6 5s^1$	800	$19 \times 19 \times 12$
Re	$5p^6 6s^1 5d^6$	600	$19 \times 19 \times 12$
Ru	$4s^2 4p^6 4d^7 5s^1$	900	$17 \times 17 \times 11$
Os	$5p^6 6s^1 5d^7$	600	$17 \times 17 \times 11$
Co	$3s^2 3p^6 4s^1 3d^8$	900	$19 \times 19 \times 12$
Zn	$3d^{10} 4s^2$	700	$17 \times 17 \times 11$
Cd	$4d^{10} 5s^2$	700	$17 \times 17 \times 09$
Tl	$5d^{10} 6s^2 6p^1$	900	$17 \times 17 \times 11$

TABLE I: Parameters for atomic relaxation simulations performed using VASP in the PBE approximation for the exchange-correlation functional. E_{cut} is the plane wave cut-off energy and k -grid denotes the Γ -centered evenly spaced k point mesh utilized for a two-atom hcp primitive cell.

and the point defect structures were relaxed until the maximum magnitude of force on any atom was smaller than 0.01 eV/Å. The Perdew-Burke-Ernzerhof (PBE) exchange-correlation functional E_{xc} [51] was employed for all the hcp elements. For Be, Zn and Cd, the PBEsol functional [52] was also considered, as discussed in section III. Otherwise, earlier studies have shown that various choices for E_{xc} often do not have a significant effect on the resulting elastic dipole tensors [2, 3].

Bulk lattice parameters were optimised such that the change in energy between the successive ionic relaxation steps in calculations of perfect lattice structures was less than 10^{-7} eV. As shown in Figure 2, the predicted lattice parameters are in good agreement with experiment data [44], and the relative error of either a or c with respect to experiment does not exceed 5%. Furthermore, the predicted c/a ratios differ from experimental values by less than 3%.

The elastic constants were computed *via* the symmetrised finite differences method [58, 59]. In general, the relative differences between the predicted and measured elastic constants [53–57] are satisfactory. The largest relative error appears in the C_{12} elastic constant of Be, for which the experimental value is $C_{12} = 27.6$ GPa [53]. We note, however, that the absolute error in this case is still similar to the scale of discrepancies found across all the hcp elements.

Ferromagnetic hcp Co was treated in the collinear magnetic approximation, similarly to the treatment of ferromagnetic bcc Fe and antiferromagnetic bcc Cr [2], and ferromagnetic fcc Ni [3]. The calculated magnetic mo-

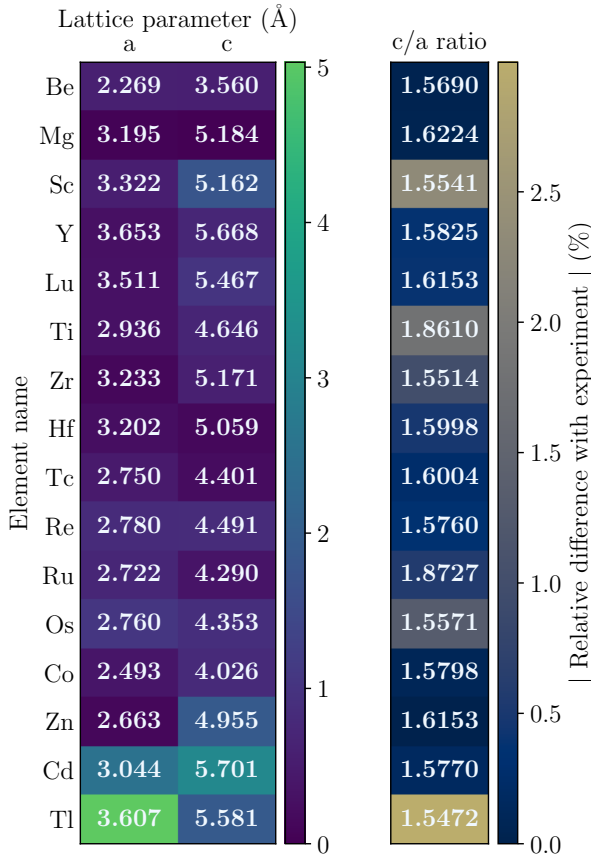


FIG. 2: *Ab initio* predicted values of lattice parameters and c/a ratios for all the hcp elements included in this study. The cells in the table are coloured according to the absolute difference between the calculated values and experimental measurements. Experiment data are sourced from Ref. [44] and are the 0K values, with the exception of Hf for which the lowest temperature experimental values correspond to room temperature.

ment of $1.616 \mu_B$ per Co atom is in good agreement with the experimentally measured value of $1.71 \mu_B$ per atom [60].

The formation energies $E_{\text{def}}^{\text{F}}$ and elastic dipole tensors of a vacancy and five self interstitial atom defect configurations were computed for each chemical element. The formation energy of a defect is defined as

$$E_{\text{def}}^{\text{F}} = [E_{\text{def}}(N_{\text{def}}) - E^{\text{app}}] - \frac{N_{\text{def}}}{N_{\text{perf}}} E_{\text{perf}}(N_{\text{perf}}) - E_{\text{el}}^{\text{corr}}, \quad (1)$$

where the energy of a simulation cell containing a defect in a configuration of the total of N_{def} atoms is E_{def} , and the corresponding perfect lattice reference cell containing N_{perf} atoms is E_{perf} . For a vacancy or a self interstitial atom defect, $N_{\text{def}} - N_{\text{perf}}$ is -1 or $+1$ respectively. E^{app} is the energy associated with externally applied strain and $E_{\text{el}}^{\text{corr}}$ is the energy of elastic interaction between a defect and all the periodic images of it. Accounting for

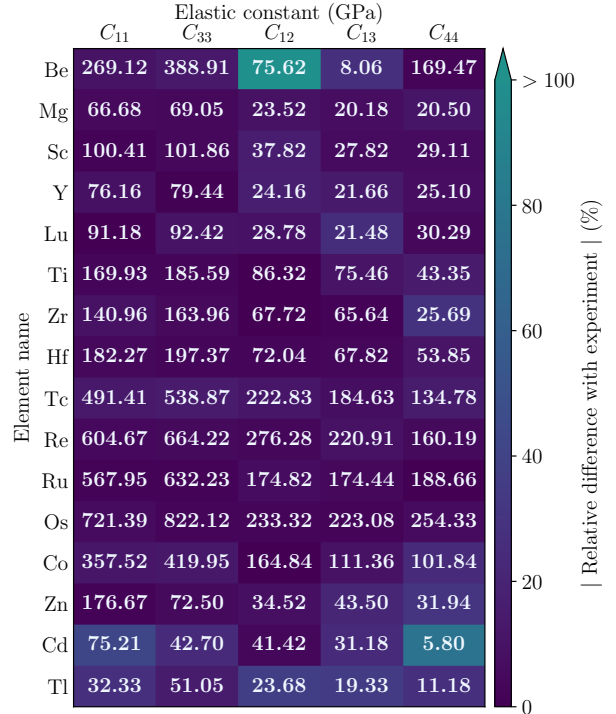


FIG. 3: *Ab initio* predicted values of elastic constants for all the hcp elements included in this study. Cells in the table are coloured according to the absolute difference between the calculated values and experimental measurements. Experiment data are sourced from Simmons, Gene and Wang, Herbert [53] for temperatures less than 4K for all the elements, with the exception of Lu [54] (4K), Os [55] (5K), Sc [56] (300 K) and Tc [57] (298 K).

the energy of interaction with periodic images of a defect structures $E_{\text{el}}^{\text{corr}}$ is possible [61], and the corresponding correction term was computed using the CALANIE program [62]. Further details may be found in Refs. [2, 3].

We constructed simulation cells from repeats of the 2 atom hcp primitive cell with space group 194 $P6_3/mmc$ and occupied Wyckoff position $c = (1/3, 2/3, 1/4)$ [63, ch. 2.3]. Both atoms in the primitive cell belong to the orbit of a single Wyckoff position. It follows that the structure and tensorial properties of a vacancy at either site in the primitive cell are related by a symmetry operation of the crystal space group. Thus, there is only one type of vacancy defect in an hcp crystal. Conversely, multiple non-equivalent SIA geometries need to be considered. The relaxed configurations of the basal octahedral (BO), basal $\langle 2\bar{1}\bar{1} \rangle$ split dumbbell (BS), octahedral (O), $\langle 0001 \rangle$ split dumbbell (BS) and crowdion (C) SIAs for Zr are shown in figure 4. Vérité *et al.* [13] and Pasianot [12] have highlighted the important role of low-symmetry defect configurations in determining the migration pathways of SIAs. For certain low symmetry configurations, the formation energy was found to be only slightly above the lowest en-

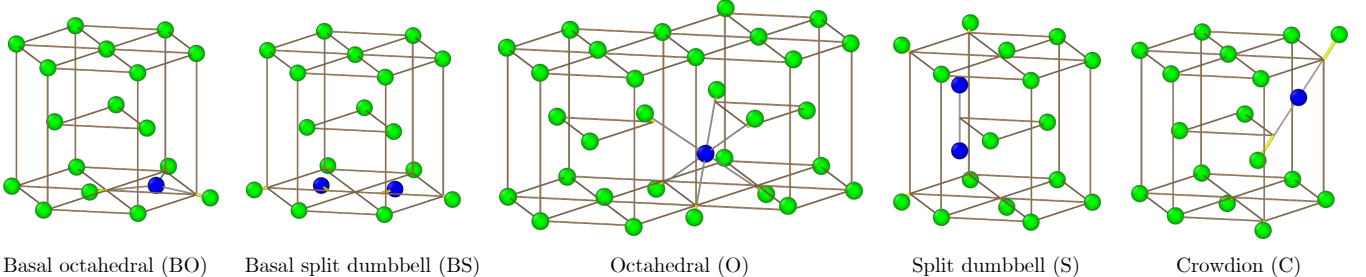


FIG. 4: From left to right: relaxed configurations of the basal octahedral (BO), basal [2 $\bar{1}$ 10] split dumbbell (BS), octahedral (O), [0001] split dumbbell (BS) and crowdion (C) SIAs for Zr. The inserted atom, or a pair of dumbbell atoms sharing an atomic site, are highlighted in blue. Atomic displacements from the initial configuration are indicated by yellow arrows.

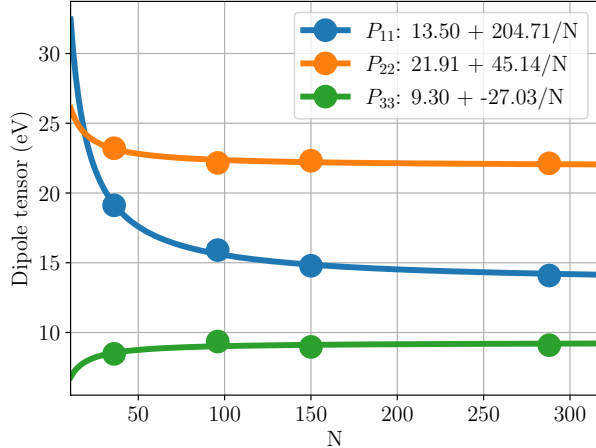


FIG. 5: Example linear extrapolation of dipole tensor components with respect to N , where N denotes the number of atoms in the reference supercell, for a basal [2 $\bar{1}$ 10] split dumbbell SIA defect in Zr. Cell shape and volume are fixed during internal atomic relaxation. The $1/N$ variation comes from the fact that interaction of a defect with its periodically translated images varies as the inverse cube of linear dimensions of the cell [61, 64].

ergy high symmetry SIA configuration. Here, we present only the high symmetry initial configurations so that the configurational and energy landscape of SIAs across all the hcp metals may be explored efficiently. As reported by Pasianot [12], we often found that the high symmetry tetrahedral, basal tetrahedral and basal crowdion defects are unstable or have relatively high formation energies. These configurations were not included in this study.

Consider a simulation cell containing a single point defect in a cell containing the total of N_{def} atoms. The structure of the defect is relaxed under the condition that the cell shape and size are fixed. The dipole tensor $P_{ij}(N_{def})$ is then evaluated from the average residual stress in the cell $\bar{\sigma}_{ij}$ as [61, 65]

$$P_{ij}(N_{def}) = -V\bar{\sigma}_{ij}, \quad (2)$$

where V is the volume of the cell. Asymptotically, the stress field of a defect varies as the inverse cube of the distance from its centre $\|\sigma_{ij}(\mathbf{r})\| \sim 1/r^3$ [4]. Hence, each defect configuration was relaxed using at least three cells containing different number of atoms N . The dipole tensor components were then extrapolated to the limit of infinite cell size to obtain the asymptotic values P_{ij}^∞ via a least squares fit with respect to a linear function of $1/N$ such that [38, 64]

$$P_{ij}(N) = \frac{\alpha_{ij}}{N} + P_{ij}^\infty, \quad (3)$$

where α_{ij} is a fitted constant. Often we found that the reference supercell representing the relaxed perfect crystal contains some remnant stress, stemming from the approximations involved in the numerical relaxation procedure. In this way, we have computed the stress of the initial perfect crystal supercell and subtracted it from the elastic interaction-corrected dipole tensor for each cell size before performing the $1/N$ extrapolation. The number of repeats along each lattice vector were chosen such that the cell edge lengths were approximately equal, resulting in 36, 96 and 150 atom cells arising from the $3 \times 3 \times 2$, $4 \times 4 \times 3$, $5 \times 5 \times 3$ unit cell repeats respectively. Where computational resources were available, relaxations were also performed on larger cell sizes. Due to the large c/a ratio of Zn and Cd, a 64-atom $4 \times 4 \times 2$ cell was considered in place of a 96 atom $4 \times 4 \times 3$ cell. For many of the transition hcp metals, we found that Eq. 3 provided a good fit to the point defect data. However, Be, Mg, Zn, Cd and Tl presented less optimal fits. In order to maintain consistency, we have presented the result of applying the procedure described above to all elements.

Relaxation volume tensors of isolated point defects Ω_{ij} were computed from the corresponding extrapolated dipole tensors P_{ij}^∞ via

$$\Omega_{ij} = S_{ijkl}P_{ij}^\infty. \quad (4)$$

Unless stated otherwise, we express Ω_{ij} in the atomic volume units Ω_0 for the respective hcp metal, where for

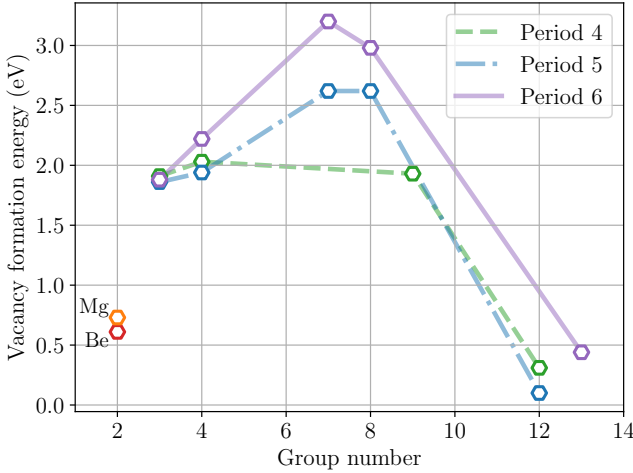


FIG. 6: Formation energies of vacancies in hcp metals plotted as a function of the group number of the respective chemical element in the Periodic Table.

the hcp crystal structure $\Omega_0 = \frac{\sqrt{3}}{4}a^2c$. Example extrapolations for the elastic dipole tensors of a Zr vacancy and a Zn crowdion are shown in figure 5. Extrapolations for other elements and defect configurations are given in the Supplementary Material.

III. RESULTS

The formation energies E_f , elastic dipole tensors P_{ij} and relaxation volume tensors Ω_{ij} for point defects across all hcp metals highlighted in FIG. 1 are summarised in Tables II - XX. In sections III A and III B, we analyse the properties of vacancies and SIAs respectively. Our values for the dipole and relaxation volume tensors of defects included in the study by Pasianot [12] agree with the values computed there.

A. Vacancies

The vacancy formation energies found in our study agree with those computed by Shang *et al.* [18] within 0.2 eV for all the elements except beryllium where our value for the vacancy formation energy $E_F^{\text{Vac}} = 0.16$ eV is significantly lower than 0.92 eV found in Ref. [18, Table 3]. The discrepancy may be a result of our choice of E_{cut} , k -point mesh density or choice of Be pseudopotential. Here we used $E_{\text{cut}} = 800$ eV compared to $E_{\text{cut}} = 1.4 \times \text{ENMAX} = 345$ eV where ENMAX is the recommended cut-off supplied in the Be POTCAR file, or 432 eV for the Be_sv POTCAR.

The relaxation volume tensor of a vacancy in an hcp

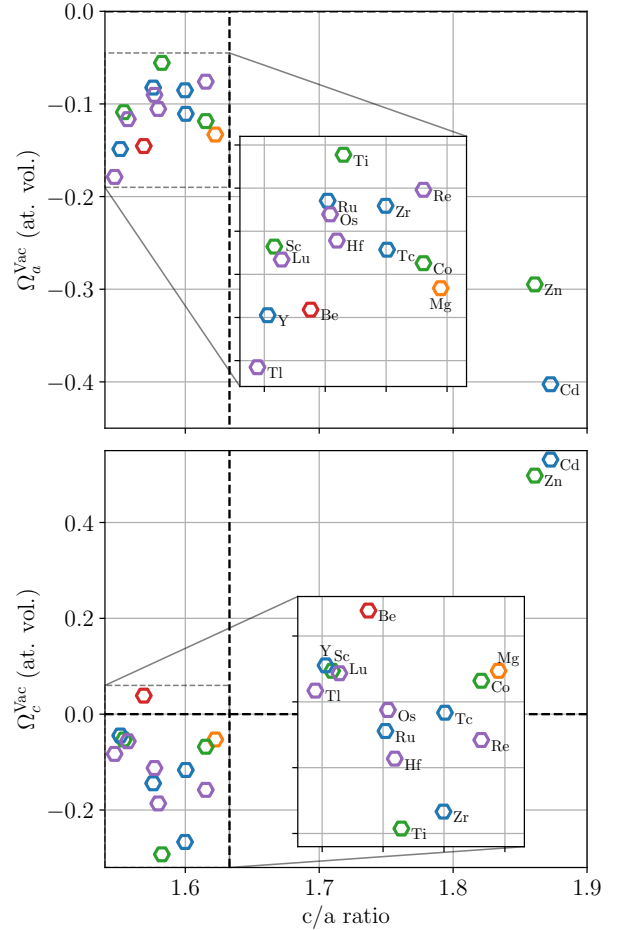


FIG. 7: Vacancy relaxation volume tensor components Ω_a and Ω_c , defined in equation 5 with respect to the hcp crystallographic coordinate system. Vertical dashed lines indicate the ideal ratio $c/a = \sqrt{8/3}$.

crystal has the form [38]

$$\boldsymbol{\Omega}^{\text{Vac}} = \begin{pmatrix} \Omega_a^{\text{Vac}} & 0 & 0 \\ 0 & \Omega_a^{\text{Vac}} & 0 \\ 0 & 0 & \Omega_c^{\text{Vac}} \end{pmatrix}, \quad (5)$$

for independent strains in the basal plane Ω_a^{Vac} and along the c -axis Ω_c^{Vac} . Ω_a^{Vac} and Ω_c^{Vac} are plotted in figure 7 as a function of c/a ratio. For elements with the less than ideal c/a ratio, we observe a weak positive correlation. We also note that Ω_c^{Vac} is found to be positive for Cd and Zn, despite the fact that vacancies in materials are centres of contraction. For Be, the magnitude of $\Omega_c^{\text{Vac}} = 0.039\Omega_0$ is smaller than the errors associated with the choice of the exchange-correlation functional E_{xc} and the pseudopotential. Hence, the sign of the vacancy c strain in beryllium is uncertain.

In general, a second rank tensor $\boldsymbol{\Omega}$ may be decomposed into an isotropic $\frac{1}{3}\text{Tr}(\boldsymbol{\Omega})\mathbf{I}$ and deviatoric $\boldsymbol{\Omega}^d = \boldsymbol{\Omega} - \frac{1}{3}\text{Tr}(\boldsymbol{\Omega})\mathbf{I}$ parts, where \mathbf{I} is the Kronecker delta

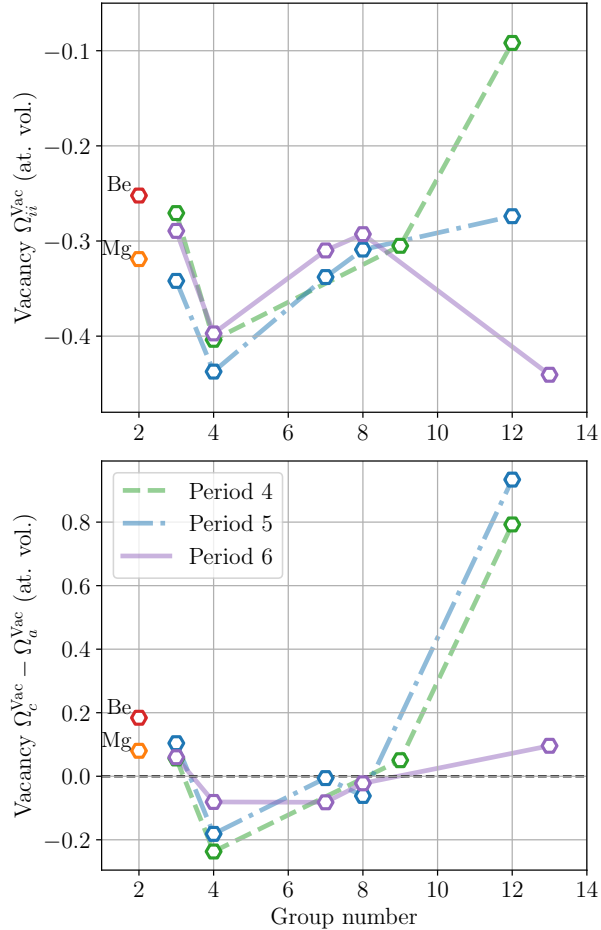


FIG. 8: Vacancy relaxation volume tensor components Ω_a and Ω_c , defined in equation 5 with respect to the hcp crystallographic coordinate system. Vertical dashed lines indicate the ideal ratio $c/a = \sqrt{8/3}$.

tensor. Hence, we may rewrite eq. 5 as

$$\boldsymbol{\Omega}^{Vac} = \frac{\Omega_{ii}^{Vac}}{3} \mathbf{I} + \frac{\Omega_c^{Vac} - \Omega_a^{Vac}}{3} \begin{pmatrix} -1 & 0 & 0 \\ 0 & -1 & 0 \\ 0 & 0 & 2 \end{pmatrix}, \quad (6)$$

where the relaxation volume Ω_{ii}^{Vac} is the trace of tensor $\boldsymbol{\Omega}^{Vac}$, and the principal shear strain $\Omega_c^{Vac} - \Omega_a^{Vac}$ is a measure of the difference in the c and a strains induced by a vacancy, and is proportional to the magnitude of the deviatoric part of $\boldsymbol{\Omega}^{Vac}$. The volumetric and shear strains are plotted in figure 8 with respect to the group number of the element in the Periodic Table. The dilatation and shear strains become more negative in elements of group IV, increasing again across a given period. Once again, the cases of Cd and Zn are anomalous, with the $\Omega_c - \Omega_a$ value being relatively large due to the substantial positive c strain.

	Self interstitial atom (SIA) configuration label				
	BO	BS	O	S	C
Be	3.90	4.21	5.13	5.28	4.33
Mg	2.26	2.34	2.29	2.25	2.16
Sc	2.02	2.54	2.39	2.92	2.71
Y	2.08	2.54	2.52	2.93	2.79
Lu	2.62	3.10	3.09	3.60	-
Ti	2.38	2.60	2.52	2.81	-
Zr	2.69	2.87	2.91	3.05	3.32
Hf	3.97	4.26	4.42	4.62	-
Tc	5.20	5.56	5.88	4.39	-
Re	7.84	8.34	8.46	6.95	-
Ru	8.48	9.15	8.52	8.43	-
Os	11.88	12.96	12.14	11.84	-
Co	4.43	4.96	5.04	4.31	-
Zn	2.97	3.07	1.24	1.37	1.25
Cd	2.15	1.73	0.96	1.03	0.93
Tl	0.98	1.04	0.95	0.92	2.26

Difference with lowest energy SIA (eV)

FIG. 9: Table of SIA formation energies across the hcp elements in the Periodic Table. For a given element, cells are coloured according to the difference between the formation energy of a configuration and the energy of the most stable SIA structure, highlighted in boldface and white borders.

B. Self interstitial atoms

In figure 9 we tabulate the formation energies of SIA configurations in hcp metals across the Periodic Table. The lowest formation energy SIA $E_{MIN}^F(\text{SIA})$ is highlighted in bold face and white border, and the cells are coloured according to the positive energy difference $E^F(\text{SIA}) - E_{MIN}^F(\text{SIA})$. SIA formation energies tend to increase towards group VIII, as shown in figure 10 where the minimum formation energy is plotted with respect to the group number. Our values for E_F are broadly in agreement with other DFT calculations for Be (**check**) [12, 20, 21], Mg [12, 40], Y [22], Ti [12, 13], Zr [13], Hf [13], Co [12], Zn [12, 19] and Cd [12]. For half of the metals with less than ideal c/a ratio, the lowest energy SIA configuration is the basal octahedral SIA. In other elements, BO is often close to the lowest energy SIA configuration. In particular, $E^F(\text{BO}) - E_{MIN}^F(\text{SIA}) \lesssim 0.1$ eV for Mg, Ru, Os, Co and Tl.

Crowdion configurations of SIA defects in hcp elements are often unstable and have high formation energies. The linear structure of a crowdion in some bcc metals, like

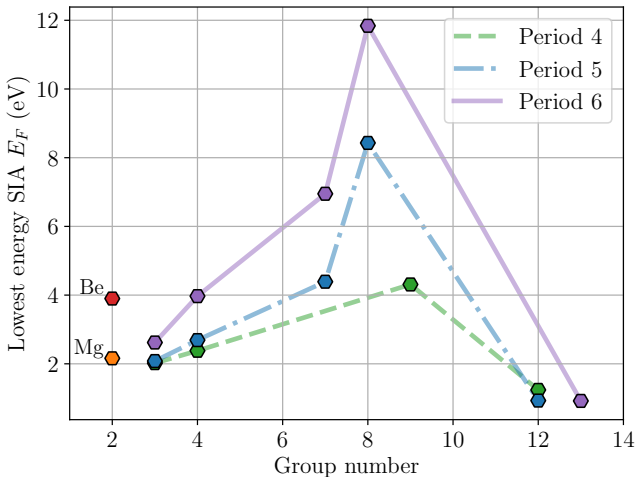


FIG. 10: The lowest self-interstitial atom defect formation energy in hcp elements with respect to the group number in the Periodic Table.

Cr, Mo and W, renders it mechanically unstable against buckling [7]. Such instabilities have also been observed in simulations of crowdion defects in group IV hcp metals Ti, Zr and Hf [13].

The formation energy differences $E_F^{\text{BS}} - E_F^{\text{BO}}$ across group III and IV metals are small. Vérité *et al.* [13] proposed that in group IV elements, SIA defects migrate through a process involving a jump from BO to a buckled crowdion or rotated split dumbbell that then glides along the c -axis before hopping to another BO configuration. $E_F^{\text{S}} - E_F^{\text{BO}}$ is higher for group III elements compared to elements of group IV and thus a BO SIA can migrate within the basal plane by alternating with BS configurations, as suggested for one of the possible migration pathways in Zr [36].

For the group II metals Sc and Y, and the lanthanide Lu, resistivity recovery experiments have shown the onset of stage I_D recovery to be at temperatures T_{1D} between 105 to 130 K [66, §2.4]. This corresponds to migration energies of ~ 0.3 eV and, within the uncertainties of the simulation and experiment, it is not clear whether this is consistent with the lowest formation energy difference of $\sim 0.4 - 0.5$ eV found in our simulation.

Our calculations suggest that the most stable SIA in Mg adopts the crowdion configuration. However, the difference between the formation energy of a crowdion and any other SIA configuration is less than 0.2 eV. Therefore, it is difficult to determine the lowest energy SIA with complete certainty, and verify predictions against experimental information. Otherwise, we observe that the similarity of formation energies implies that the hcp crystal lattice of Mg is essentially indifferent to the configuration adopted by an extra atom. Furthermore, this also implies that the SIA migration is isotropic. A similar picture of SIA migration emerges in thallium where, with the exception of a crowdion, the formation energies

of all the SIA configurations are the same within 0.12 eV.

Tc and Re in group VII have lower than ideal c/a ratio and yet, despite this, the basal octahedral SIA has a large formation energy. The high energy BO, BS and O configurations, together with an unstable crowdion structure imply that SIAs migrate through the rotation of low symmetry dumbbells or buckled crowdions as described by Vérité *et al.* [13]. Understandably, there is little experimental information available on the radioactive element Tc. For the remaining group VII hcp metal, Re, the SIA migration enthalpy of 0.16 eV has been measured experimentally [66]. This differs significantly from our lowest value $E^F(\text{SIA}) - E^F_{\text{MIN}}(\text{SIA})$ value of 0.89 eV. The existence of a lower symmetry rotated dumbbell that has the formation energy close to that of S is possible, or the observed low migration energy may be associated with impurities and imperfections in the Re sample.

To the best of our knowledge, no experimental information on point defect properties in elements of group VIII is available. Our data suggest that $E_f(\text{BS})$ has a high formation energy relative to the lowest energy configurations. This raises the possibility that SIAs transform between BO, O and S configurations with relative ease, biasing SIA migration along the c axis.

Magnetism in Co does not appear to produce any anomalies in the ordering of SIA formation energies. Given the lower than ideal c/a ratio of cobalt, the formation energy of the BO configuration is still low.

Zn and Cd exhibit relatively high formation energies for the basal plane SIAs, whereas the E_F values for O, S and C configurations are similar. This implies that the diffusion of SIAs occurs rapidly along the c -axis and relatively slow in the basal plane. There is a great deal of uncertainty in modelling Zn and Cd using DFT as many exchange-correlation functionals are unable to describe correlations in the d -electron shell with sufficient accuracy [67]. Furthermore, we found that even the predicted lattice parameters and elastic constants of Zn and Cd are highly sensitive to the k -point mesh employed. We repeated our calculations for Cd with the PBEsol E_{xc} functional [52] and found that the formation energy of a crowdion defect was markedly different, with the formation energy of 2.75 eV and the lowest formation energy configuration of the defect instead being an octahedral SIA. However, the energy of the basal configuration remained significantly higher than that for the inter-basal plane SIAs.

In figure 11 we show (0001) cross-sections of electron charge density difference (ECDD) for the basal octahedral SIAs in Be, Mg, Zr, Re, and Zn. Despite belonging to the same group, Be and Mg exhibit very different bonding characters that are highly anisotropic and isotropic respectively. The d -orbital bonding is apparent for Zr and Re whereas the ellipsoidal regions of charge depletion in Zn arises from the completed d shell. While the ECDD maps are consistent with the expected bonding in these metals, they do not immediately provide an explanation for the relative stability of different SIA con-

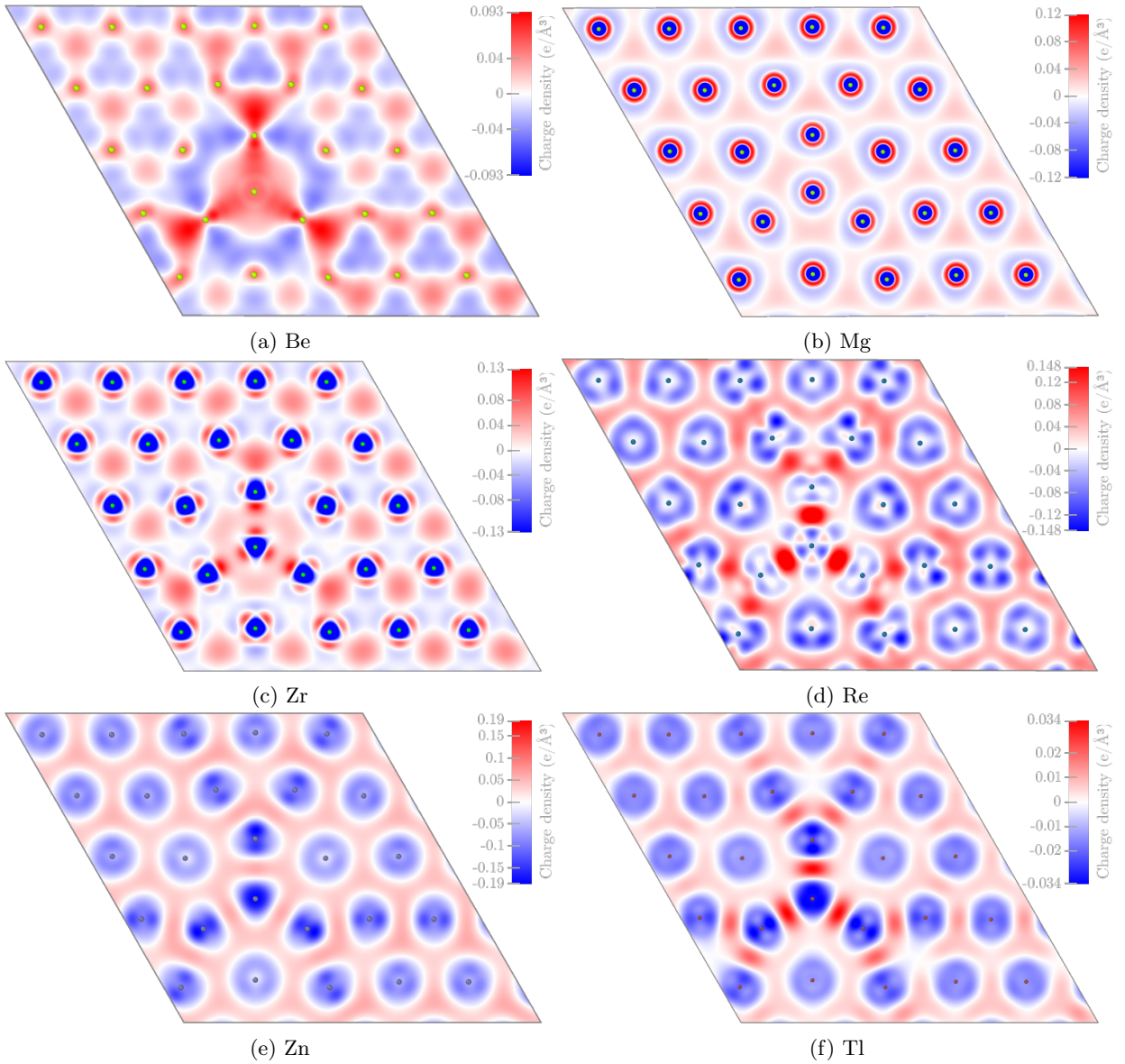


FIG. 11: BO SIA defect electron charge density difference (ECDD) for Be, Mg, Zr, Re, Zn and Tl. The position of atoms within the slice are rendered as spheres.

figurations. We note that a similar lack of direct correspondence between the type of interatomic bonding and the structure of defects was found in bcc metals [2].

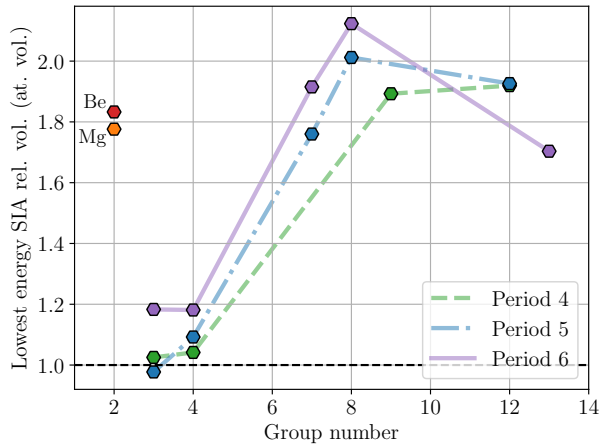
The relaxation volumes and magnitude of deviatoric tensors for the lowest formation energy interstitials computed for various chemical elements are plotted in figure 12. In a given group, the relaxation volume increases from period 4 to period 6 with the exception of elements of group III. Across a given period, the relaxation volume peaks at group VIII. With the exception of group XII, the magnitudes of deviatoric tensors across the hcp transition metals are similar.

Huang diffuse X-ray scattering experiments provide information about the invariants of dipole tensors of low energy SIAs. In particular, the anisotropy ratio P_{33}/P_a

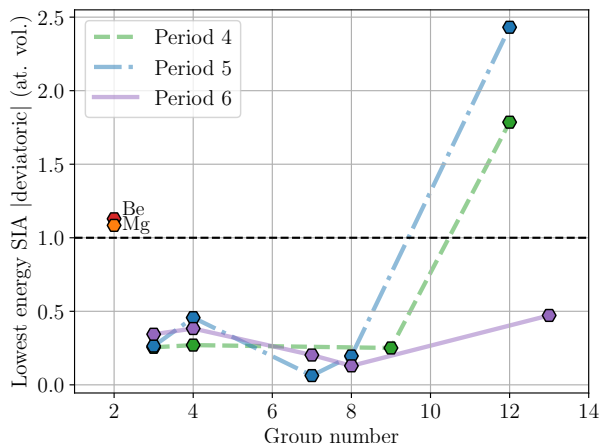
is often reported for hcp metals [12, 68] where it is defined as

$$P_a = \sqrt{[2(P_{11}^2 + P_{22}^2 + 2P_{12}^2) + (P_{11} + P_{22})^2]/8}. \quad (7)$$

Values of parameter P_a for the lowest formation energy SIA configurations are plotted in figure 13 as a function of the group number. There is a positive linear correlation along the *d*-block. However, we caution that the anisotropy ratio varies strongly as a function of defect configuration and thus, particularly where there is uncertainty as to the true lowest energy SIA, different exchange correlation functionals may produce qualitatively different trends. No discernable trend could be identified with respect to the c/a ratio of a given metal.



(a)



(b)

FIG. 12: Relaxation volumes and the magnitude of relaxation volume deviatoric tensor for the lowest energy SIA defect for each element shown in figure 9.

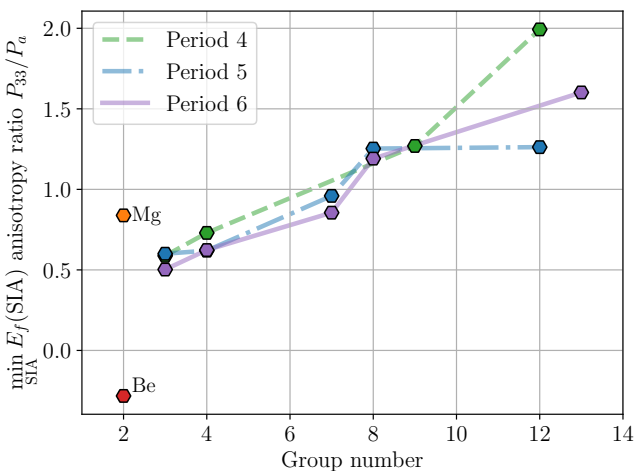
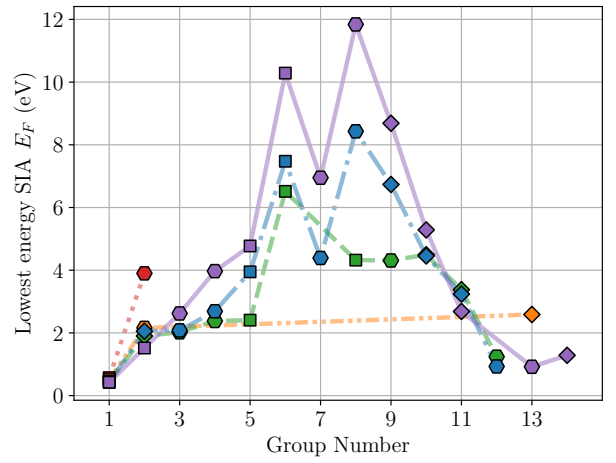
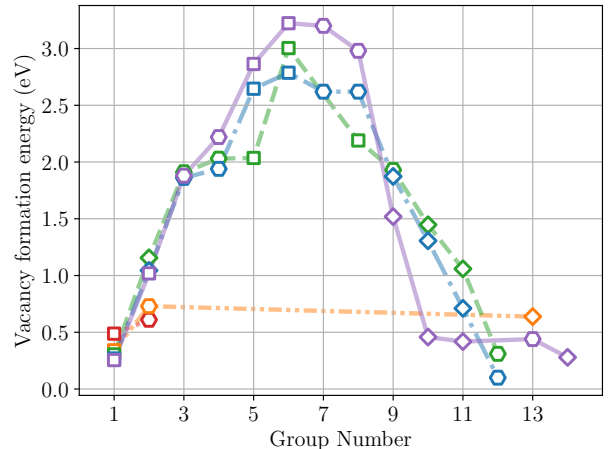


FIG. 13: Plot of dipole tensor anisotropy ratio for the lowest energy SIA as a function of the Periodic Table group number for a given element.



(a)



(b)

FIG. 14: Point defect formation energies for SIAs (a) and vacancies (b) across all the bcc, fcc and hcp metals.

IV. HCP, BCC AND FCC METALS

All the new data on point defect relaxation volumes computed for hcp metals have now been combined with the data on bcc [2] and fcc [3] data to provide a comprehensive review of properties of defects across the Periodic Table. We compare results obtained using the PBE functional across all the datasets for consistency, and owing to the fact that it was predominantly the PBE functional that was employed across all the elements.

The formation energies of vacancies and lowest energy SIAs are plotted in figure 14. The formation energy E_F increases towards the middle of the transition metal block for both types of point defects, with slight variation in the location of the peak between the periods and point defect types. Across the third period, vacancy and SIA formation energies are maximum at antiferromagnetic Cr in group VI. The largest vacancy formation energy is also at group VI for Mo and W in periods 4 and 5, respec-

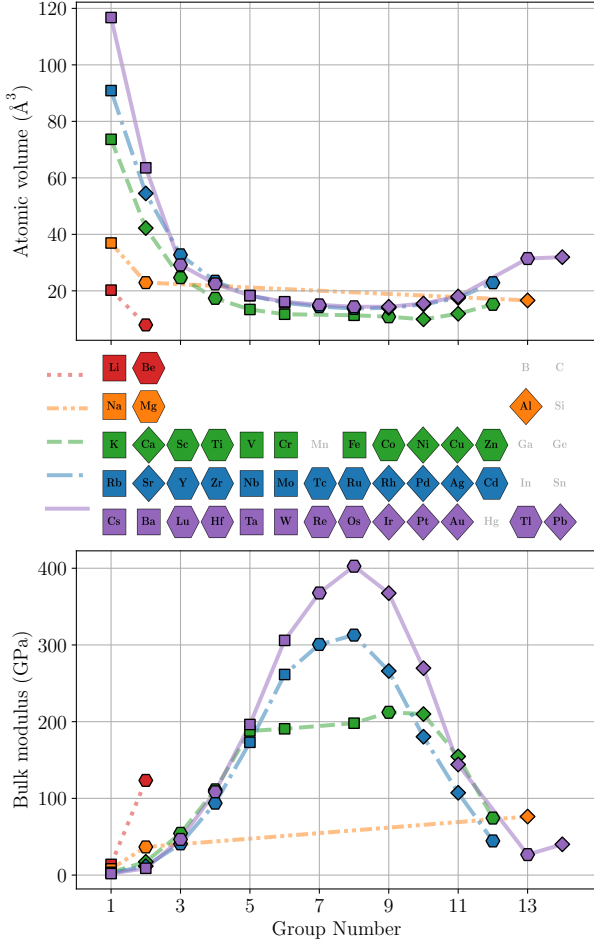


FIG. 15: Variation of atomic volume (top) and bulk modulus (bottom) as a function of group number in the Periodic Table for all the bcc, fcc and hcp elements.

tively. For the self-interstitial atom defects, $E_F(\text{SIA})$ instead drops substantially at group VII for Tc and Re, before rising slightly at Ru and Os in group VIII.

These trends with respect to changes in the electronic structure of metals are somewhat similar to the variation of their bulk moduli. In particular, figure 15 shows that metals become stiffer towards the middle of the transition block. Conversely, the atomic volume is also minimum at that point.

In figure 16, vacancy and SIA relaxation volumes are plotted as functions of element's group number. On average, vacancy and self-interstitial atom defect relaxation volumes in pure elements fluctuate around ~ -0.35 and ~ 1.46 atomic volumes, respectively. For comparison, in the limit where defects form clusters, for example voids or dislocation loops, the relaxation volume *per defect* asymptotically approaches -1 atomic volume for vacancy dislocation loops, $+1$ atomic volume for interstitial dislocation loops, and zero for voids [69].

Variation of relaxation volumes of point defects across a given period is similar to other periods. Oscillatory

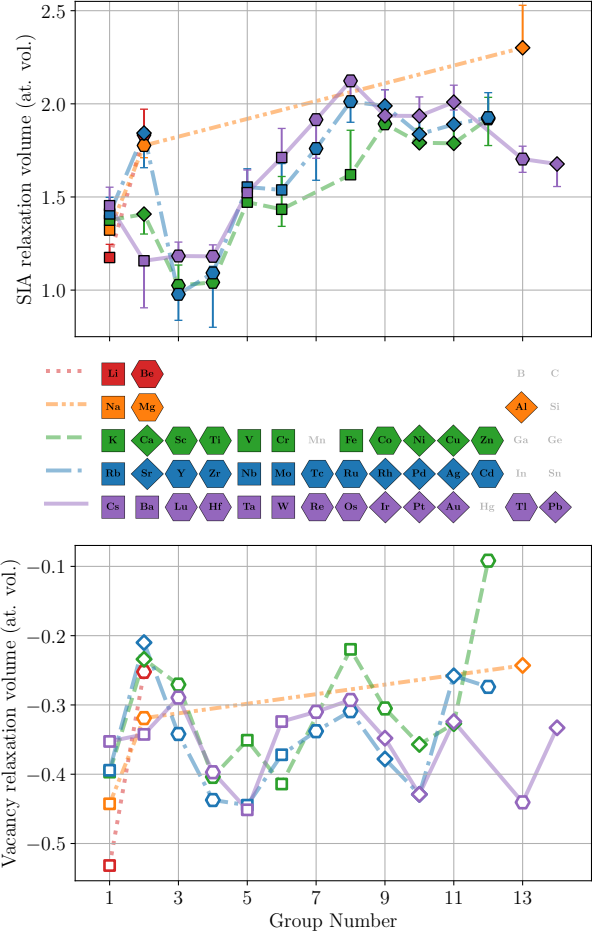


FIG. 16: Vacancy relaxation volumes for hcp (this work), bcc [2] and fcc [3] metals. Data for fcc Th have been excluded and hcp Lu was treated as a group 3 element. Error bars indicate the largest and smallest SIA relaxation volume for all the simulated configurations.

behaviour is observed for vacancies with distinct peaks and troughs in group II, V and VIII with the exception of bcc vanadium. Self-interstitial atom defects also show a similar variation across periods, although the oscillation period is larger, with a distinct peak and trough at groups VIII and III, respectively.

Figure 17 shows a strong correlation between the relaxation volume of a defect and the atomic volume of the respective element. The relaxation volumes of vacancies Ω_{Vac} and the most stable SIAs Ω_{SIA} are well approximated by

$$\Omega_{\text{Vac}} \sim -0.35\Omega \quad (8)$$

$$\Omega_{\text{SIA}} \sim +1.46\Omega, \quad (9)$$

where Ω is the atomic volume. The coefficient of determination R^2 for both linear fits is 0.93.

The Voigt averaged bulk modulus B provides a good approximation for the pressure $p = -\frac{1}{3}\sigma_{ii}$ and stress ten-

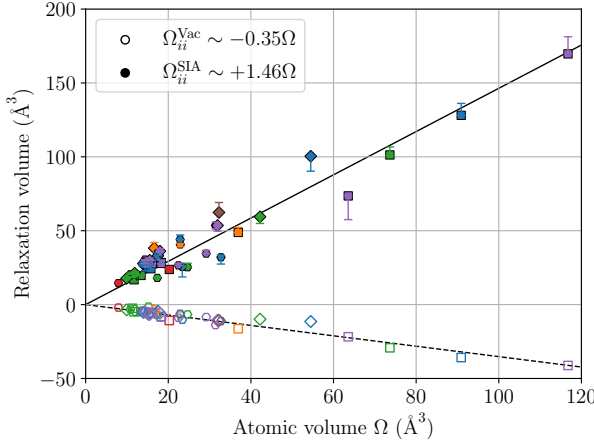


FIG. 17: Traces of SIA and vacancy relaxation volume tensors Ω_{ii} for hcp (this work), bcc [2] and fcc [3] metals plotted against the atomic volume for the respective element. Data points show Ω_{ii} for the lowest energy SIA configurations, and the error bars indicate the range of variation of defect volumes across all the SIA configurations for that element.

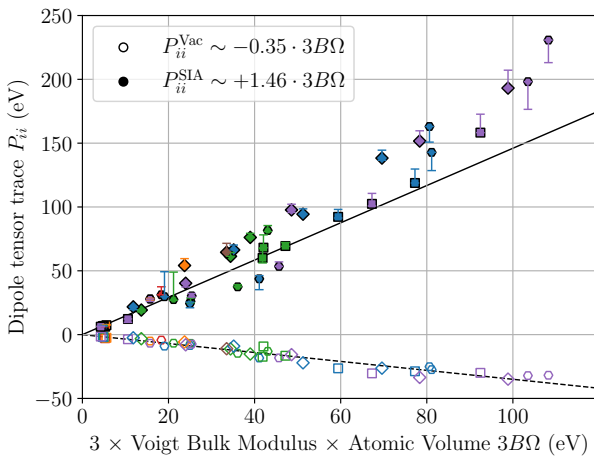


FIG. 18: Traces of SIA and vacancy elastic dipole tensors P_{ii} for hcp (this work), bcc [2] and fcc [3] metals plotted against the product of the bulk modulus and atomic volume for the respective element. Data points show P_{ii}^{SIA} for the lowest energy SIA configurations, and the error bars indicate the range of variation of defect dipole tensors across all the SIA configurations for that element.

sor σ_{ij} arising from dilatation Δ such that

$$p = B\Delta, \quad (10)$$

where equation 10 is exact for cubic metals. Therefore, from equation 9 it follows that the trace of the dipole tensor for vacancies, P_{ii}^{Vac} , and SIAs, P_{ii}^{SIA} is expected to

scale linearly with bulk modulus according to

$$P_{ii}^{\text{Vac}} \sim -0.35 \cdot 3B\Omega \quad (11)$$

$$P_{ii}^{\text{SIA}} \sim +1.46 \cdot 3B\Omega, \quad (12)$$

assuming that the linear regression deduced in equation 9 is satisfied. The correlation between the trace of elastic dipole tensor of a defect and the product of the bulk modulus and atomic volume is illustrated in figure 18. The coefficient of determination R^2 for SIA and vacancies dipole tensor trace linear fits are 0.86 and 0.93, respectively. The gradient of 1.79 presents a better fit for the SIA dipole tensor trace, yielding $R^2 = 0.94$.

No notable trends were identified for the anisotropic parts of the dipole and relaxation volume tensors with respect to electron configuration. This suggests that the anisotropic properties of point defects in metals is most strongly affected by the crystal structure. For example, bcc and fcc vacancies contain no deviatoric components in either their dipole or relaxation volume tensors [2, 3]. However, in hcp metals the deviatoric part can be substantial as discussed in section III A.

V. CONCLUSIONS

In this study, we computed elastic dipole and relaxation volume tensors of intrinsic point defects across all the hcp metals in the periodic table. This completes the *ab initio* database of point defect properties of hcp, bcc and fcc metals [2, 3] across the Periodic Table, save the lanthanides and actinides. SIA defects show little variation in their relaxation volumes for the configurations considered; it remains to be seen whether lower symmetry configurations break this trend. For both interstitials and vacancies, we have found a strong correlation between the traces of relaxation volume tensors and dipole tensors with atomic volume and bulk modulus of respective elements. The data reviewed in this study can now be used for predicting radiation-induced deformation [70] of metals both currently in service in nuclear power plants and those yet to be tested in extreme radiation environments.

ACKNOWLEDGMENTS

The authors gratefully acknowledge stimulating discussions with M. Boleininger and D. R. Mason. This work has been carried out within the framework of the EUROfusion Consortium, funded by the European Union via the Euratom Research and Training Programme (Grant Agreement No. 101052200—EUROfusion), and was partially supported by the Broader Approach Phase II agreement under the PA of IFERC2-T2PA02. This work was also funded by the UK Fusion Futures Programme and the UK EPSRC Energy Programme (Grant Number EP/W006839/1). To obtain further information on

TABLE II: Beryllium (Be) point defect dipole tensor data computed using the GGA-PBE functional. Formation energy E_f is given in eV units, dipole tensor components P_{ij} also in eV units, and relaxation volume tensor components Ω_{ij} and its trace $\Omega_{rel} = \Omega_{ii}$ are given in atomic volume units.

Be_PBE	E_f	P_{11}	P_{22}	P_{33}	P_{12}	P_{23}	P_{31}	Ω_{11}	Ω_{22}	Ω_{33}	Ω_{12}	Ω_{23}	Ω_{31}	Ω_{rel}
Vac	0.610	-4.004	-4.004	3.684	0.000	0.000	0.000	-0.239	-0.239	0.201	0.000	0.000	0.000	-0.277
BO	3.900	18.692	18.692	-5.766	0.000	0.000	0.000	1.103	1.103	-0.345	0.000	0.000	0.000	1.861
BS	4.210	19.214	18.008	-5.331	0.000	0.000	0.000	1.161	1.035	-0.322	0.000	0.000	0.000	1.873
C	4.330	21.923	12.302	0.273	5.402	8.208	9.356	1.505	0.501	-0.027	1.127	0.978	1.115	1.979
O	5.130	16.508	16.508	1.730	0.000	0.000	0.000	0.966	0.966	0.050	0.000	0.000	0.000	1.981
S	5.280	7.500	7.500	23.420	0.000	0.000	0.000	0.411	0.411	1.199	0.000	0.000	0.000	2.021

TABLE III: Beryllium (Be) point defect dipole tensor data computed using the GGA-PBEsol functional. Formation energy E_f is given in eV units, dipole tensor components P_{ij} also in eV units, and relaxation volume tensor components Ω_{ij} and its trace $\Omega_{rel} = \Omega_{ii}$ are given in atomic volume units.

Be_PBEsol	E_f	P_{11}	P_{22}	P_{33}	P_{12}	P_{23}	P_{31}	Ω_{11}	Ω_{22}	Ω_{33}	Ω_{12}	Ω_{23}	Ω_{31}	Ω_{rel}
Vac	0.580	-4.787	-4.787	5.004	0.000	0.000	0.000	-0.277	-0.277	0.260	0.000	0.000	0.000	-0.294
BO	4.250	15.675	15.675	-1.025	0.000	0.000	0.000	0.901	0.901	-0.065	0.000	0.000	0.000	1.736
BS	4.350	16.399	16.441	-1.371	0.000	0.000	0.000	0.942	0.945	-0.084	0.000	0.000	0.000	1.803
C	4.470	18.945	11.035	4.037	4.742	6.850	8.214	1.104	0.615	0.194	0.586	0.852	1.022	1.912
S	5.340	3.666	3.666	30.178	0.000	0.000	0.000	0.198	0.198	1.539	0.000	0.000	0.000	1.935
O	5.500	14.647	14.647	4.058	0.000	0.000	0.000	0.839	0.839	0.195	0.000	0.000	0.000	1.874

the data and models underlying the paper please contact PublicationsManager@ukaea.uk. Views and opinions expressed are however those of the authors only and do not necessarily reflect those of the European Union or the European Commission. Neither the European Union nor the European Commission can be held responsible for them. Numerical calculations were performed using resources provided by the Cambridge Service for Data Driven Discovery (CSD3) operated by the University of Cambridge Research Computing Service and ARCHER 2, the UK National Supercomputing Service.

Appendix A: Convergence testing

Here we detail convergence tests for all of the hexagonal close packed (hcp) metals discussed in the main text. Each figure from figure 19 to 37 shows the results of convergence tests and elastic dipole tensor extrapolations for a given element using the Perdew-Burke-Ernzerhof (PBE) exchange correlation functional. Where the PBEsol was considered this is stated after the element name for Be, Cd and Zn in separate figures.

For each element, the plane wave energy cut-off E_{cut} and k -point mesh data are shown in subfigures (a) and (b). The convergence tests were conducted as follows. A primitive hcp unit cell containing two atoms had the atom $(1/3, 2/3, 1/4)$ displaced by 0.1 \AA along the x direction. The k -point mesh was fixed as E_{cut} was varied in subfigure (a) and E_{cut} was fixed as the k -point mesh was varied. k meshes $k_a \times k_a \times k_c$ were Γ -centred and chosen

such that the ratio of grid points along the basal plane reciprocal lattice vectors k_a to the number of points along the c direction k_c was approximately equal to the experimental c/a ratio of the given hcp metal. A single self-consistent field (SCF) cycle was subsequently carried out. The energy per atom (eV), [2110] component of force on the displaced atom (eV/ \AA) and the 11 component of the unit cell stress were recorded for each SCF calculation. For all elements, we attempted to choose E_{cut} and the k -point mesh so that the energy per atom, force and stress quantities were converged to at least 1 meV per atom, 1 meV/ \AA and 0.5 kBar respectively. Where this could not be achieved, we subsequently chose the highest plane wave cut-off and/or densest k -point mesh tested.

Subfigures (c) and above show the dipole tensor calculations for vacancy and self-interstitial atom defects. Where a SIA was unstable and did not relax satisfactorily the corresponding plots are not included.

TABLE IV: Magnesium (Mg) point defect dipole tensor data computed using the GGA-PBE functional. Formation energy E_f is given in eV units, dipole tensor components P_{ij} also in eV units, and relaxation volume tensor components Ω_{ij} and its trace $\Omega_{rel} = \Omega_{ii}$ are given in atomic volume units.

Mg_PBE	E_f	P_{11}	P_{22}	P_{33}	P_{12}	P_{23}	P_{31}	Ω_{11}	Ω_{22}	Ω_{33}	Ω_{12}	Ω_{23}	Ω_{31}	Ω_{rel}
Vac	0.730	-1.869	-1.869	-1.290	0.000	0.000	0.000	-0.133	-0.133	-0.053	0.000	0.000	0.000	-0.319
C	2.160	10.891	8.752	8.332	0.566	1.853	0.980	0.832	0.485	0.459	0.183	0.632	0.334	1.776
S	2.250	9.085	9.085	9.946	0.000	0.000	0.000	0.551	0.551	0.685	0.000	0.000	0.000	1.787
BO	2.260	12.178	12.178	2.695	0.000	0.000	0.000	1.016	1.016	-0.321	0.000	0.000	0.000	1.711
O	2.290	8.737	8.737	10.935	0.000	0.000	0.000	0.494	0.494	0.819	0.000	0.000	0.000	1.807
BS	2.340	15.305	9.885	2.418	0.000	0.000	0.000	1.499	0.621	-0.375	0.000	0.000	0.000	1.746

TABLE V: Scandium (Sc) point defect dipole tensor data computed using the GGA-PBE functional. Formation energy E_f is given in eV units, dipole tensor components P_{ij} also in eV units, and relaxation volume tensor components Ω_{ij} and its trace $\Omega_{rel} = \Omega_{ii}$ are given in atomic volume units.

Sc_PBE	E_f	P_{11}	P_{22}	P_{33}	P_{12}	P_{23}	P_{31}	Ω_{11}	Ω_{22}	Ω_{33}	Ω_{12}	Ω_{23}	Ω_{31}	Ω_{rel}
Vac	1.910	-2.543	-2.543	-1.761	0.000	0.000	0.000	-0.109	-0.109	-0.053	0.000	0.000	0.000	-0.271
BO	2.020	10.059	10.059	5.910	0.000	0.000	0.000	0.446	0.446	0.133	0.000	0.000	0.000	1.025
O	2.390	9.102	9.102	8.233	0.000	0.000	0.000	0.362	0.362	0.327	0.000	0.000	0.000	1.051
BS	2.540	11.615	9.543	7.533	0.000	0.000	0.000	0.558	0.342	0.235	0.000	0.000	0.000	1.135
C	2.710	7.081	6.969	13.423	0.724	0.097	1.255	0.183	0.172	0.759	0.150	0.022	0.280	1.114
S	2.920	4.125	4.125	16.727	0.000	0.000	0.000	-0.023	-0.023	1.080	0.000	0.000	0.000	1.033

TABLE VI: Yttrium (Y) point defect dipole tensor data computed using the GGA-PBE functional. Formation energy E_f is given in eV units, dipole tensor components P_{ij} also in eV units, and relaxation volume tensor components Ω_{ij} and its trace $\Omega_{rel} = \Omega_{ii}$ are given in atomic volume units.

Y_PBE	E_f	P_{11}	P_{22}	P_{33}	P_{12}	P_{23}	P_{31}	Ω_{11}	Ω_{22}	Ω_{33}	Ω_{12}	Ω_{23}	Ω_{31}	Ω_{rel}
Vac	1.860	-3.247	-3.247	-2.041	0.000	0.000	0.000	-0.149	-0.149	-0.045	0.000	0.000	0.000	-0.342
BO	2.080	9.379	9.379	5.632	0.000	0.000	0.000	0.433	0.433	0.110	0.000	0.000	0.000	0.977
O	2.520	8.432	8.432	7.859	0.000	0.000	0.000	0.348	0.348	0.294	0.000	0.000	0.000	0.989
BS	2.540	10.827	8.130	6.514	0.000	0.000	0.000	0.553	0.299	0.169	0.000	0.000	0.000	1.020
C	2.790	6.482	6.061	12.364	1.148	0.364	1.989	0.180	0.140	0.674	0.216	0.071	0.388	0.994
S	2.930	2.994	2.994	15.058	0.000	0.000	0.000	-0.061	-0.061	0.961	0.000	0.000	0.000	0.838

TABLE VII: Lutetium (Lu) point defect dipole tensor data computed using the GGA-PBE functional. Formation energy E_f is given in eV units, dipole tensor components P_{ij} also in eV units, and relaxation volume tensor components Ω_{ij} and its trace $\Omega_{rel} = \Omega_{ii}$ are given in atomic volume units.

Lu_PBE	E_f	P_{11}	P_{22}	P_{33}	P_{12}	P_{23}	P_{31}	Ω_{11}	Ω_{22}	Ω_{33}	Ω_{12}	Ω_{23}	Ω_{31}	Ω_{rel}
Vac	1.880	-2.765	-2.765	-1.863	0.000	0.000	0.000	-0.116	-0.116	-0.057	0.000	0.000	0.000	-0.289
BO	2.620	12.130	12.130	6.094	0.000	0.000	0.000	0.535	0.535	0.113	0.000	0.000	0.000	1.183
O	3.090	10.255	10.255	10.617	0.000	0.000	0.000	0.389	0.389	0.450	0.000	0.000	0.000	1.227
BS	3.100	14.979	10.097	7.139	0.000	0.000	0.000	0.758	0.328	0.172	0.000	0.000	0.000	1.258
S	3.600	5.830	5.830	17.760	0.000	0.000	0.000	0.085	0.085	1.015	0.000	0.000	0.000	1.185

TABLE VIII: Titanium (Ti) point defect dipole tensor data computed using the GGA-PBE functional. Formation energy E_f is given in eV units, dipole tensor components P_{ij} also in eV units, and relaxation volume tensor components Ω_{ij} and its trace $\Omega_{rel} = \Omega_{ii}$ are given in atomic volume units.

Ti_PBE	E_f	P_{11}	P_{22}	P_{33}	P_{12}	P_{23}	P_{31}	Ω_{11}	Ω_{22}	Ω_{33}	Ω_{12}	Ω_{23}	Ω_{31}	Ω_{rel}
Vac	2.030	-3.933	-3.933	-6.786	0.000	0.000	0.000	-0.056	-0.056	-0.293	0.000	0.000	0.000	-0.404
BO	2.380	13.722	13.722	10.015	0.000	0.000	0.000	0.458	0.458	0.126	0.000	0.000	0.000	1.042
O	2.520	13.816	13.816	11.418	0.000	0.000	0.000	0.435	0.435	0.215	0.000	0.000	0.000	1.085
BS	2.600	10.426	18.336	9.335	0.000	0.000	0.000	0.065	0.939	0.057	0.000	0.000	0.000	1.060
S	2.810	10.169	10.169	18.430	0.000	0.000	0.000	0.127	0.127	0.814	0.000	0.000	0.000	1.068

TABLE IX: Zirconium (Zr) point defect dipole tensor data computed using the GGA-PBE functional. Formation energy E_f is given in eV units, dipole tensor components P_{ij} also in eV units, and relaxation volume tensor components Ω_{ij} and its trace $\Omega_{rel} = \Omega_{ii}$ are given in atomic volume units.

Zr_PBE	E_f	P_{11}	P_{22}	P_{33}	P_{12}	P_{23}	P_{31}	Ω_{11}	Ω_{22}	Ω_{33}	Ω_{12}	Ω_{23}	Ω_{31}	Ω_{rel}
Vac	1.940	-5.156	-5.156	-8.022	0.000	0.000	0.000	-0.085	-0.085	-0.267	0.000	0.000	0.000	-0.437
BO	2.690	16.694	16.694	10.344	0.000	0.000	0.000	0.551	0.551	-0.009	0.000	0.000	0.000	1.092
BS	2.870	13.627	21.842	9.409	0.000	0.000	0.000	0.229	0.997	-0.098	0.000	0.000	0.000	1.128
O	2.910	14.795	14.795	16.624	0.000	0.000	0.000	0.357	0.357	0.408	0.000	0.000	0.000	1.122
S	3.050	11.084	11.084	21.505	0.000	0.000	0.000	0.108	0.108	0.811	0.000	0.000	0.000	1.028
C	3.320	10.049	2.706	22.461	0.478	6.359	0.828	0.228	-0.458	1.030	0.089	1.695	0.221	0.800

TABLE X: Hafnium (Hf) point defect dipole tensor data computed using the GGA-PBE functional. Formation energy E_f is given in eV units, dipole tensor components P_{ij} also in eV units, and relaxation volume tensor components Ω_{ij} and its trace $\Omega_{rel} = \Omega_{ii}$ are given in atomic volume units.

Hf_PBE	E_f	P_{11}	P_{22}	P_{33}	P_{12}	P_{23}	P_{31}	Ω_{11}	Ω_{22}	Ω_{33}	Ω_{12}	Ω_{23}	Ω_{31}	Ω_{rel}
Vac	2.220	-5.529	-5.529	-7.159	0.000	0.000	0.000	-0.105	-0.105	-0.186	0.000	0.000	0.000	-0.397
BO	3.970	20.379	20.379	12.701	0.000	0.000	0.000	0.550	0.550	0.081	0.000	0.000	0.000	1.181
BS	4.260	17.488	25.202	11.591	0.000	0.000	0.000	0.347	0.846	0.009	0.000	0.000	0.000	1.202
O	4.420	17.554	17.554	21.859	0.000	0.000	0.000	0.345	0.345	0.553	0.000	0.000	0.000	1.243
S	4.620	12.616	12.616	30.220	0.000	0.000	0.000	0.077	0.077	1.040	0.000	0.000	0.000	1.193

TABLE XI: Technetium (Tc) point defect dipole tensor data computed using the GGA-PBE functional. Formation energy E_f is given in eV units, dipole tensor components P_{ij} also in eV units, and relaxation volume tensor components Ω_{ij} and its trace $\Omega_{rel} = \Omega_{ii}$ are given in atomic volume units.

Tc_PBE	E_f	P_{11}	P_{22}	P_{33}	P_{12}	P_{23}	P_{31}	Ω_{11}	Ω_{22}	Ω_{33}	Ω_{12}	Ω_{23}	Ω_{31}	Ω_{rel}
Vac	2.620	-9.049	-9.049	-9.326	0.000	0.000	0.000	-0.111	-0.111	-0.116	0.000	0.000	0.000	-0.338
S	4.390	48.246	48.246	46.296	0.000	0.000	0.000	0.612	0.612	0.535	0.000	0.000	0.000	1.760
BO	5.200	52.274	52.274	26.679	0.000	0.000	0.000	0.816	0.816	-0.009	0.000	0.000	0.000	1.623
BS	5.560	57.215	46.418	24.881	0.000	0.000	0.000	1.042	0.595	-0.048	0.000	0.000	0.000	1.590
O	5.880	37.384	37.384	64.750	0.000	0.000	0.000	0.287	0.287	1.139	0.000	0.000	0.000	1.713

TABLE XII: Rhenium (Re) point defect dipole tensor data computed using the GGA-PBE functional. Formation energy E_f is given in eV units, dipole tensor components P_{ij} also in eV units, and relaxation volume tensor components Ω_{ij} and its trace $\Omega_{rel} = \Omega_{ii}$ are given in atomic volume units.

Re_PBE	E_f	P_{11}	P_{22}	P_{33}	P_{12}	P_{23}	P_{31}	Ω_{11}	Ω_{22}	Ω_{33}	Ω_{12}	Ω_{23}	Ω_{31}	Ω_{rel}
Vac	3.200	-9.555	-9.555	-12.995	0.000	0.000	0.000	-0.076	-0.076	-0.158	0.000	0.000	0.000	-0.310
S	6.950	69.410	69.410	59.367	0.000	0.000	0.000	0.721	0.721	0.473	0.000	0.000	0.000	1.915
BO	7.840	74.735	74.735	33.057	0.000	0.000	0.000	0.926	0.926	-0.085	0.000	0.000	0.000	1.766
BS	8.340	92.354	56.586	27.551	0.000	0.000	0.000	1.529	0.368	-0.189	0.000	0.000	0.000	1.708
O	8.460	53.148	53.148	86.902	0.000	0.000	0.000	0.352	0.352	1.160	0.000	0.000	0.000	1.864

TABLE XIII: Ruthenium (Ru) point defect dipole tensor data computed using the GGA-PBE functional. Formation energy E_f is given in eV units, dipole tensor components P_{ij} also in eV units, and relaxation volume tensor components Ω_{ij} and its trace $\Omega_{rel} = \Omega_{ii}$ are given in atomic volume units.

Ru_PBE	E_f	P_{11}	P_{22}	P_{33}	P_{12}	P_{23}	P_{31}	Ω_{11}	Ω_{22}	Ω_{33}	Ω_{12}	Ω_{23}	Ω_{31}	Ω_{rel}
Vac	2.620	-7.414	-7.414	-10.303	0.000	0.000	0.000	-0.082	-0.082	-0.144	0.000	0.000	0.000	-0.309
S	8.430	50.118	50.118	62.809	0.000	0.000	0.000	0.591	0.591	0.831	0.000	0.000	0.000	2.012
BO	8.480	57.347	57.347	36.119	0.000	0.000	0.000	0.853	0.853	0.194	0.000	0.000	0.000	1.901
O	8.520	49.671	49.671	55.008	0.000	0.000	0.000	0.621	0.621	0.670	0.000	0.000	0.000	1.913
BS	9.150	65.662	46.200	41.224	0.000	0.000	0.000	1.091	0.514	0.316	0.000	0.000	0.000	1.921

TABLE XIV: Osmium (Os) point defect dipole tensor data computed using the GGA-PBE functional. Formation energy E_f is given in eV units, dipole tensor components P_{ij} also in eV units, and relaxation volume tensor components Ω_{ij} and its trace $\Omega_{rel} = \Omega_{ii}$ are given in atomic volume units.

Os_PBE	E_f	P_{11}	P_{22}	P_{33}	P_{12}	P_{23}	P_{31}	Ω_{11}	Ω_{22}	Ω_{33}	Ω_{12}	Ω_{23}	Ω_{31}	Ω_{rel}
Vac	2.980	-9.967	-9.967	-11.891	0.000	0.000	0.000	-0.090	-0.090	-0.112	0.000	0.000	0.000	-0.293
S	11.840	72.317	72.317	86.125	0.000	0.000	0.000	0.655	0.655	0.813	0.000	0.000	0.000	2.123
BO	11.880	80.930	80.930	51.224	0.000	0.000	0.000	0.897	0.897	0.208	0.000	0.000	0.000	2.002
O	12.140	69.381	69.381	82.473	0.000	0.000	0.000	0.629	0.629	0.778	0.000	0.000	0.000	2.036
BS	12.960	93.832	65.207	57.745	0.000	0.000	0.000	1.182	0.527	0.320	0.000	0.000	0.000	2.029

TABLE XV: Cobalt (Co) point defect dipole tensor data computed using the GGA-PBE functional. Formation energy E_f is given in eV units, dipole tensor components P_{ij} also in eV units, and relaxation volume tensor components Ω_{ij} and its trace $\Omega_{rel} = \Omega_{ii}$ are given in atomic volume units.

Co_PBE	E_f	P_{11}	P_{22}	P_{33}	P_{12}	P_{23}	P_{31}	Ω_{11}	Ω_{22}	Ω_{33}	Ω_{12}	Ω_{23}	Ω_{31}	Ω_{rel}
Vac	1.930	-4.697	-4.697	-3.715	0.000	0.000	0.000	-0.119	-0.119	-0.068	0.000	0.000	0.000	-0.305
S	4.310	24.955	24.955	31.679	0.000	0.000	0.000	0.529	0.529	0.836	0.000	0.000	0.000	1.893
BO	4.430	32.672	32.672	15.411	0.000	0.000	0.000	0.913	0.913	0.059	0.000	0.000	0.000	1.884
BS	4.960	39.095	29.016	14.730	0.000	0.000	0.000	1.350	0.576	0.008	0.000	0.000	0.000	1.934
O	5.040	22.934	22.934	39.569	0.000	0.000	0.000	0.397	0.397	1.183	0.000	0.000	0.000	1.978

TABLE XVI: Zinc (Zn) point defect dipole tensor data computed using the GGA-PBE functional. Formation energy E_f is given in eV units, dipole tensor components P_{ij} also in eV units, and relaxation volume tensor components Ω_{ij} and its trace $\Omega_{rel} = \Omega_{ii}$ are given in atomic volume units.

Zn_PBE	E_f	P_{11}	P_{22}	P_{33}	P_{12}	P_{23}	P_{31}	Ω_{11}	Ω_{22}	Ω_{33}	Ω_{12}	Ω_{23}	Ω_{31}	Ω_{rel}
Vac	0.310	-3.855	-3.855	0.991	0.000	0.000	0.000	-0.295	-0.295	0.498	0.000	0.000	0.000	-0.092
O	1.240	6.875	6.875	13.702	0.000	0.000	0.000	-0.089	-0.089	2.098	0.000	0.000	0.000	1.919
C	1.250	6.843	6.195	13.859	-0.467	0.561	-0.808	-0.095	-0.143	2.156	-0.069	0.185	-0.267	1.918
S	1.370	6.278	6.278	14.999	0.000	0.000	0.000	-0.180	-0.180	2.395	0.000	0.000	0.000	2.035
BO	2.970	19.986	19.986	6.317	0.000	0.000	0.000	1.073	1.073	-0.370	0.000	0.000	0.000	1.776
BS	3.070	30.173	12.273	6.529	0.000	0.000	0.000	1.810	0.483	-0.427	0.000	0.000	0.000	1.866

TABLE XVII: Zinc (Zn) point defect dipole tensor data computed using the GGA-PBESol functional. Formation energy E_f is given in eV units, dipole tensor components P_{ij} also in eV units, and relaxation volume tensor components Ω_{ij} and its trace $\Omega_{rel} = \Omega_{ii}$ are given in atomic volume units.

Zn_PBESol	E_f	P_{11}	P_{22}	P_{33}	P_{12}	P_{23}	P_{31}	Ω_{11}	Ω_{22}	Ω_{33}	Ω_{12}	Ω_{23}	Ω_{31}	Ω_{rel}
Vac	0.390	-2.556	-2.556	-3.263	0.000	0.000	0.000	-0.062	-0.062	-0.263	0.000	0.000	0.000	-0.387
O	1.460	5.342	5.342	24.263	0.000	0.000	0.000	-0.205	-0.205	2.478	0.000	0.000	0.000	2.067
S	1.660	5.109	5.109	25.349	0.000	0.000	0.000	-0.237	-0.237	2.607	0.000	0.000	0.000	2.132
BO	3.310	17.911	17.911	15.845	0.000	0.000	0.000	0.569	0.569	1.064	0.000	0.000	0.000	2.203

TABLE XVIII: Cadmium (Cd) point defect dipole tensor data computed using the GGA-PBE functional. Formation energy E_f is given in eV units, dipole tensor components P_{ij} also in eV units, and relaxation volume tensor components Ω_{ij} and its trace $\Omega_{rel} = \Omega_{ii}$ are given in atomic volume units.

Cd_PBE	E_f	P_{11}	P_{22}	P_{33}	P_{12}	P_{23}	P_{31}	Ω_{11}	Ω_{22}	Ω_{33}	Ω_{12}	Ω_{23}	Ω_{31}	Ω_{rel}
Vac	0.100	-4.338	-4.338	-0.346	0.000	0.000	0.000	-0.403	-0.403	0.531	0.000	0.000	0.000	-0.274
C	0.930	9.658	8.525	11.521	0.347	0.981	0.600	0.184	-0.051	1.792	0.144	1.185	0.725	1.926
O	0.960	9.247	9.247	11.648	0.000	0.000	0.000	0.073	0.073	1.804	0.000	0.000	0.000	1.950
S	1.030	9.054	9.054	12.606	0.000	0.000	0.000	-0.015	-0.015	2.090	0.000	0.000	0.000	2.060
BO	2.150	21.451	21.451	6.373	0.000	0.000	0.000	1.655	1.655	-1.372	0.000	0.000	0.000	1.939

TABLE XIX: Cadmium (Cd) point defect dipole tensor data computed using the GGA-PBESol functional. Formation energy E_f is given in eV units, dipole tensor components P_{ij} also in eV units, and relaxation volume tensor components Ω_{ij} and its trace $\Omega_{rel} = \Omega_{ii}$ are given in atomic volume units.

Cd_PBESol	E_f	P_{11}	P_{22}	P_{33}	P_{12}	P_{23}	P_{31}	Ω_{11}	Ω_{22}	Ω_{33}	Ω_{12}	Ω_{23}	Ω_{31}	Ω_{rel}
Vac	0.210	-4.719	-4.719	0.706	0.000	0.000	0.000	-0.308	-0.308	0.428	0.000	0.000	0.000	-0.188
O	1.310	9.835	9.835	16.713	0.000	0.000	0.000	0.022	0.022	1.849	0.000	0.000	0.000	1.894
S	1.470	9.479	9.479	17.856	0.000	0.000	0.000	-0.038	-0.038	2.046	0.000	0.000	0.000	1.970
C	2.750	15.503	16.578	30.941	-0.227	-0.931	-0.393	-0.137	-0.041	3.571	-0.040	-0.427	-0.180	3.393
BO	2.760	24.471	24.471	7.861	0.000	0.000	0.000	1.203	1.203	-0.481	0.000	0.000	0.000	1.925
BS	2.800	36.101	17.001	8.341	0.000	0.000	0.000	2.161	0.463	-0.550	0.000	0.000	0.000	2.073

TABLE XX: Thallium (Tl) point defect dipole tensor data computed using the GGA-PBE functional. Formation energy E_f is given in eV units, dipole tensor components P_{ij} also in eV units, and relaxation volume tensor components Ω_{ij} and its trace $\Omega_{rel} = \Omega_{ii}$ are given in atomic volume units.

Tl_PBE	E_f	P_{11}	P_{22}	P_{33}	P_{12}	P_{23}	P_{31}	Ω_{11}	Ω_{22}	Ω_{33}	Ω_{12}	Ω_{23}	Ω_{31}	Ω_{rel}
Vac	0.440	-2.281	-2.281	-2.188	0.000	0.000	0.000	-0.179	-0.179	-0.083	0.000	0.000	0.000	-0.441
S	0.920	7.742	7.742	12.400	0.000	0.000	0.000	0.375	0.375	0.953	0.000	0.000	0.000	1.703
O	0.950	7.565	7.565	12.663	0.000	0.000	0.000	0.341	0.341	1.005	0.000	0.000	0.000	1.688
BO	0.980	7.845	7.845	10.320	0.000	0.000	0.000	0.485	0.485	0.663	0.000	0.000	0.000	1.632
BS	1.040	11.760	6.331	9.280	0.000	0.000	0.000	2.279	-0.917	0.410	0.000	0.000	0.000	1.773

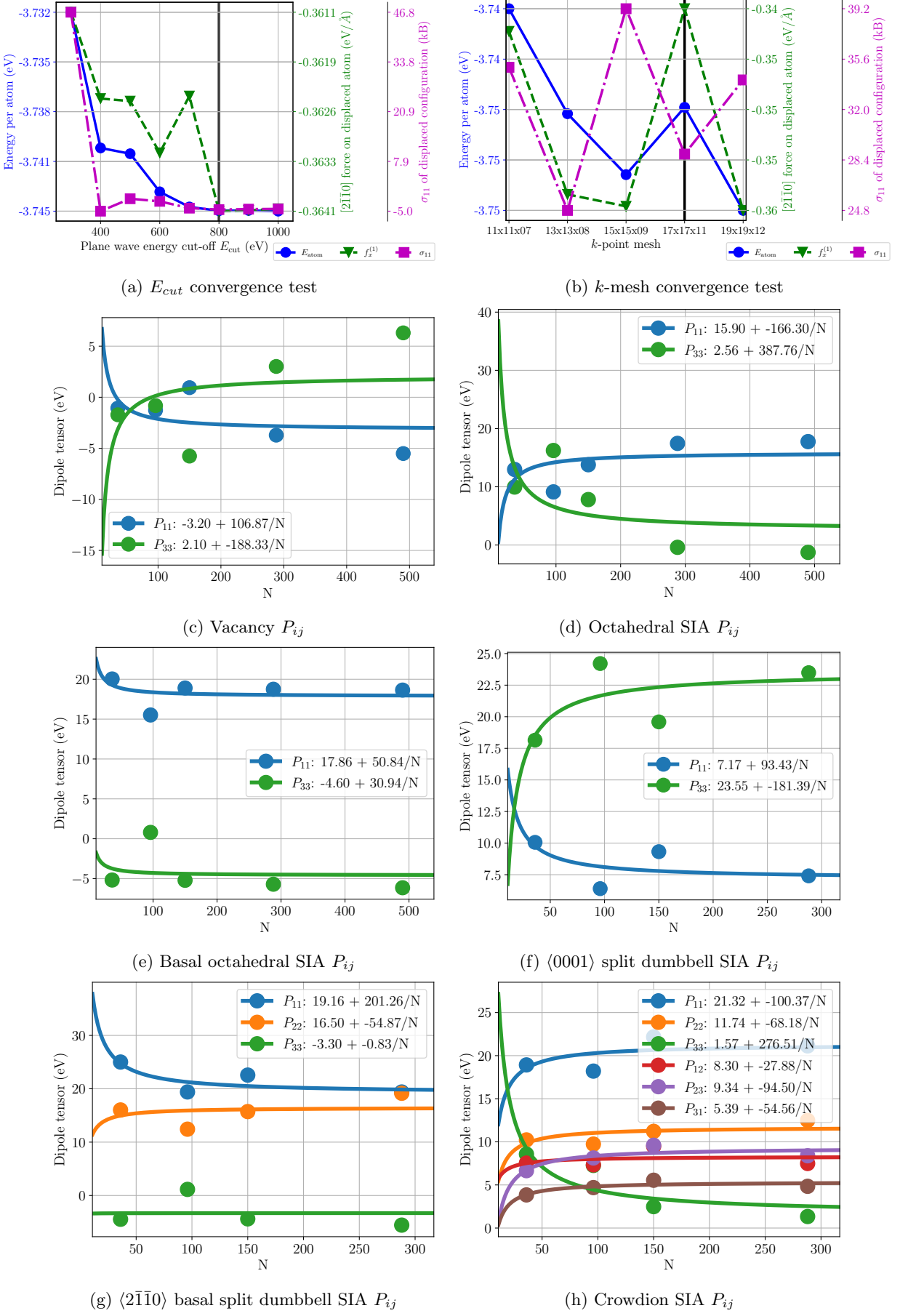


FIG. 19: Beryllium

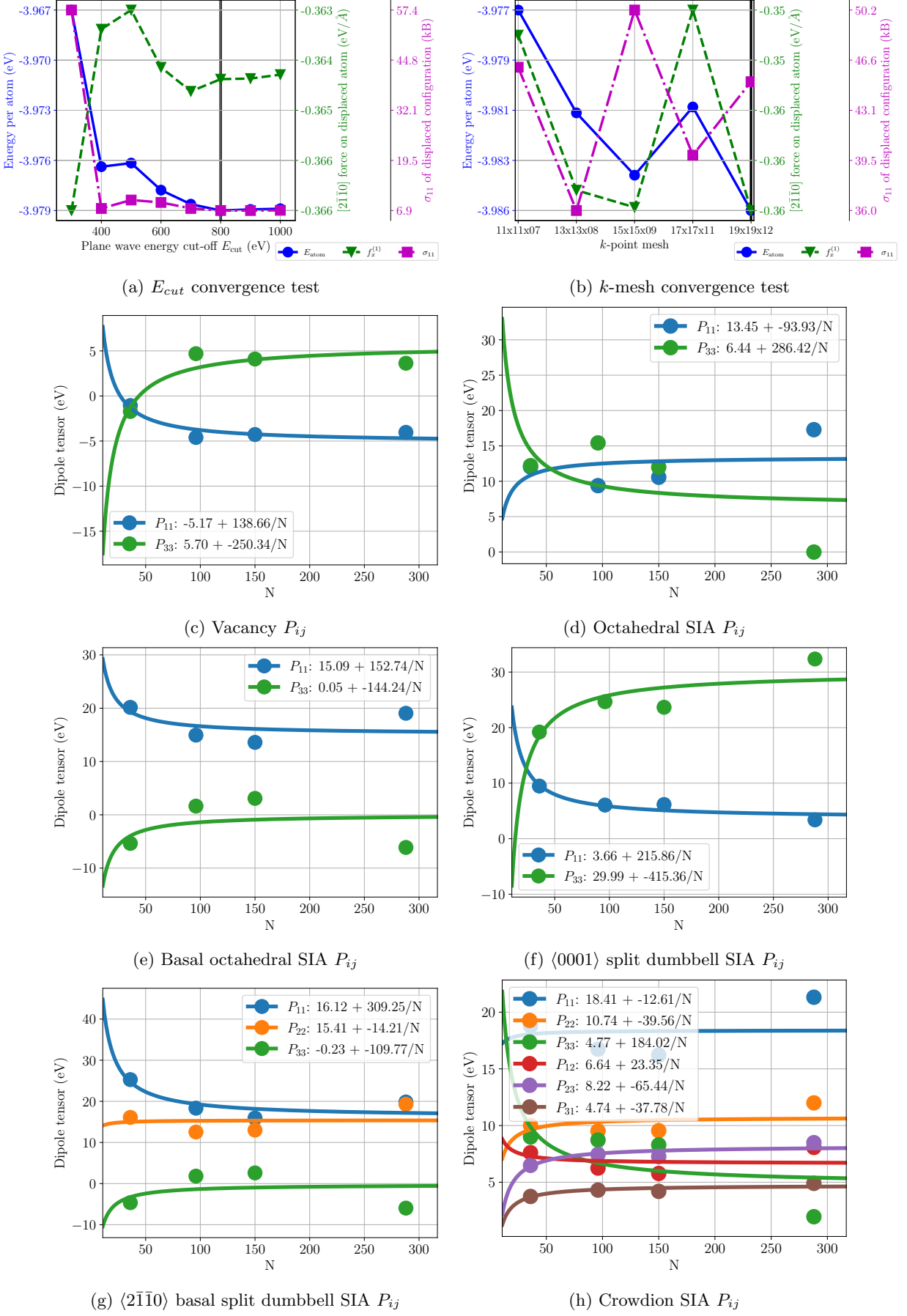


FIG. 20: Beryllium PBEsol

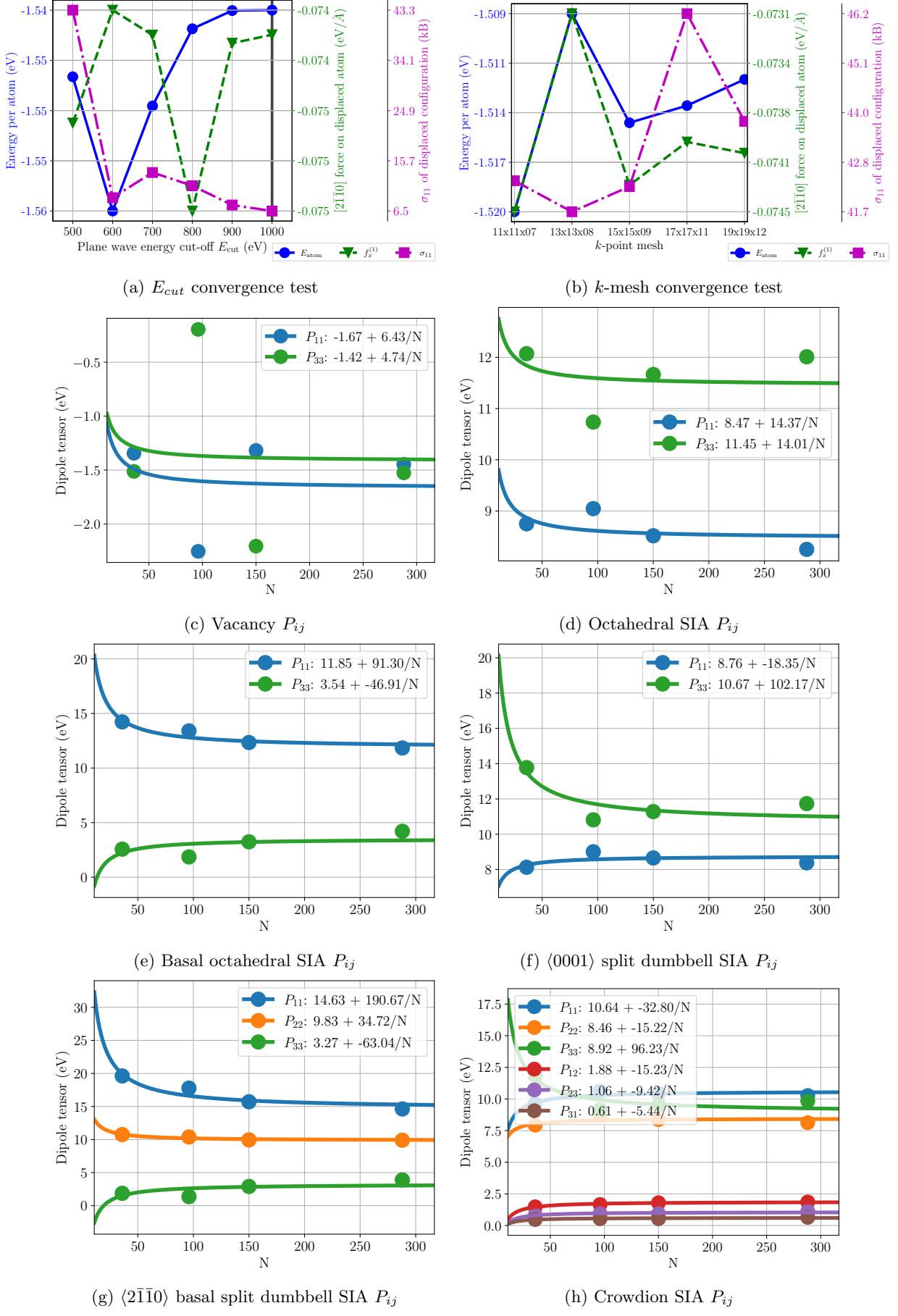


FIG. 21: Magnesium

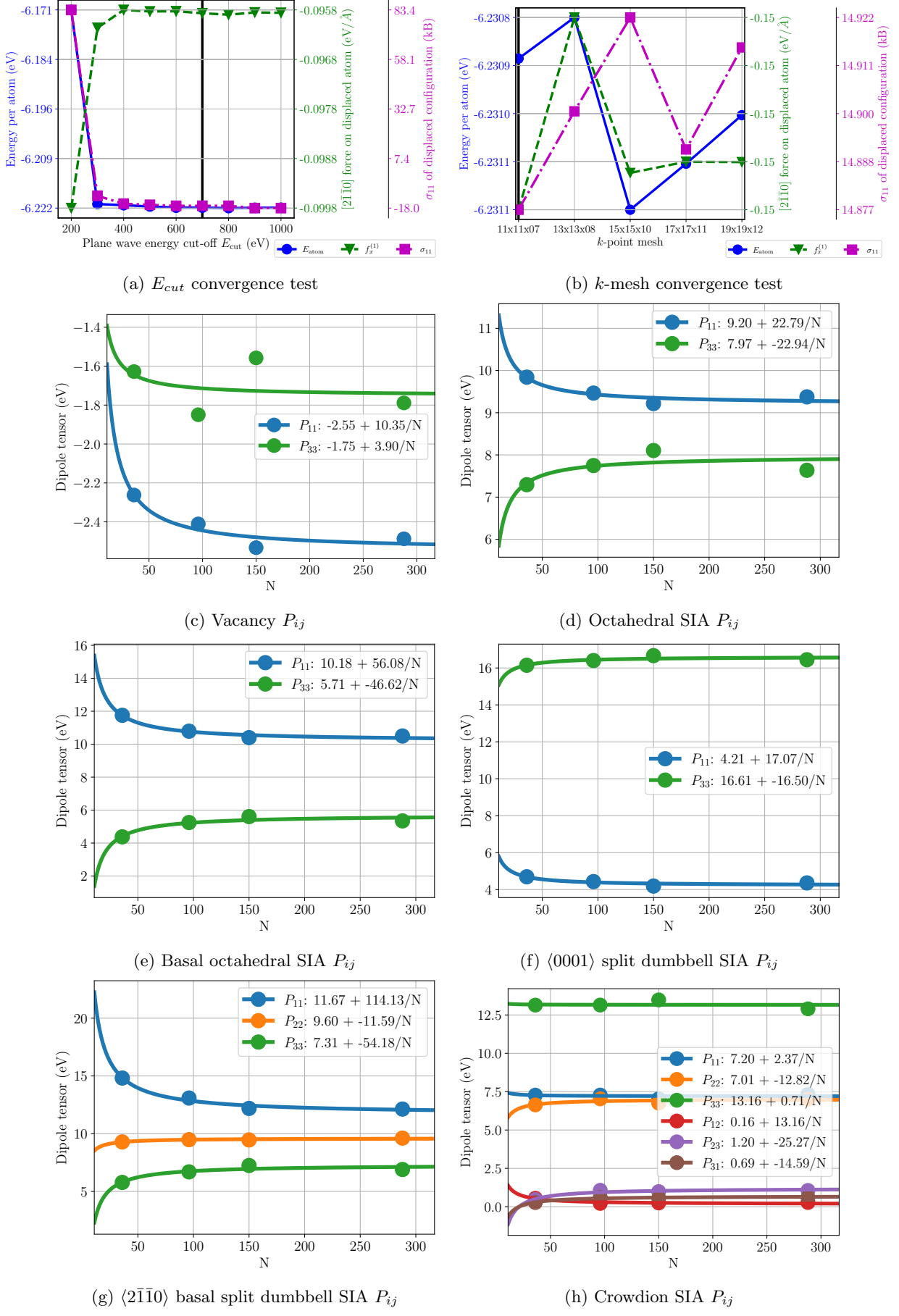


FIG. 22: Scandium

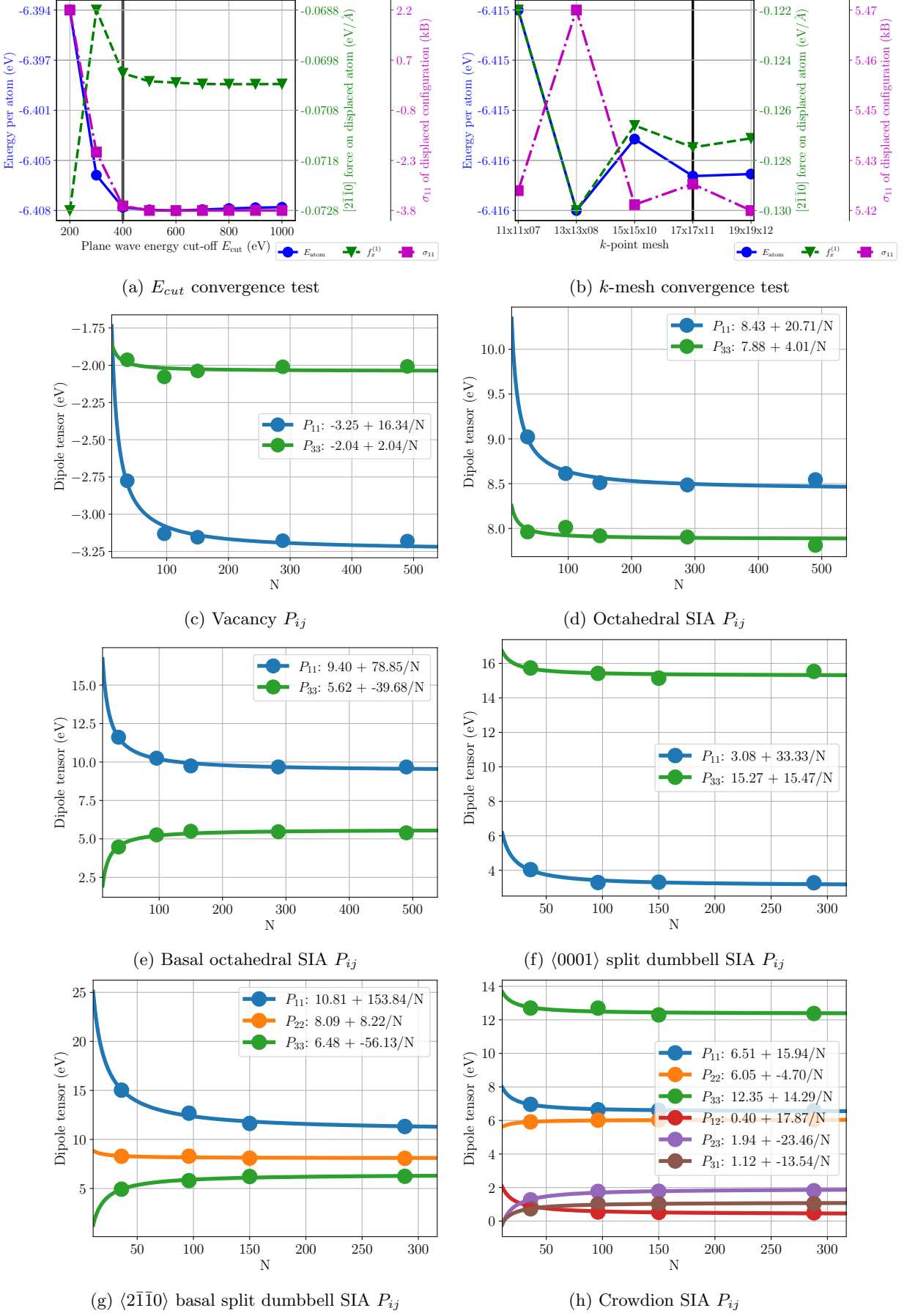


FIG. 23: Yttrium

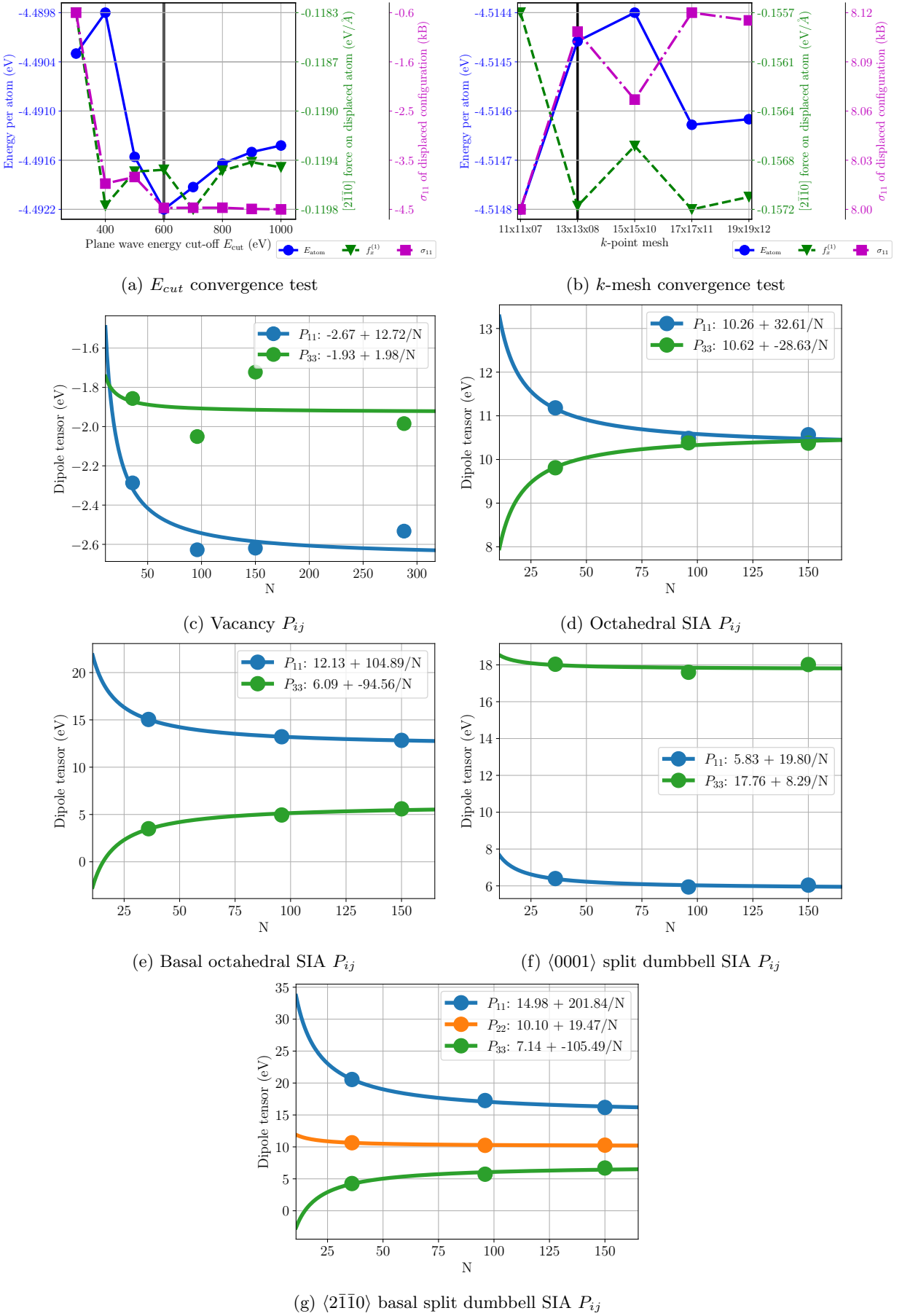


FIG. 24: Lutetium

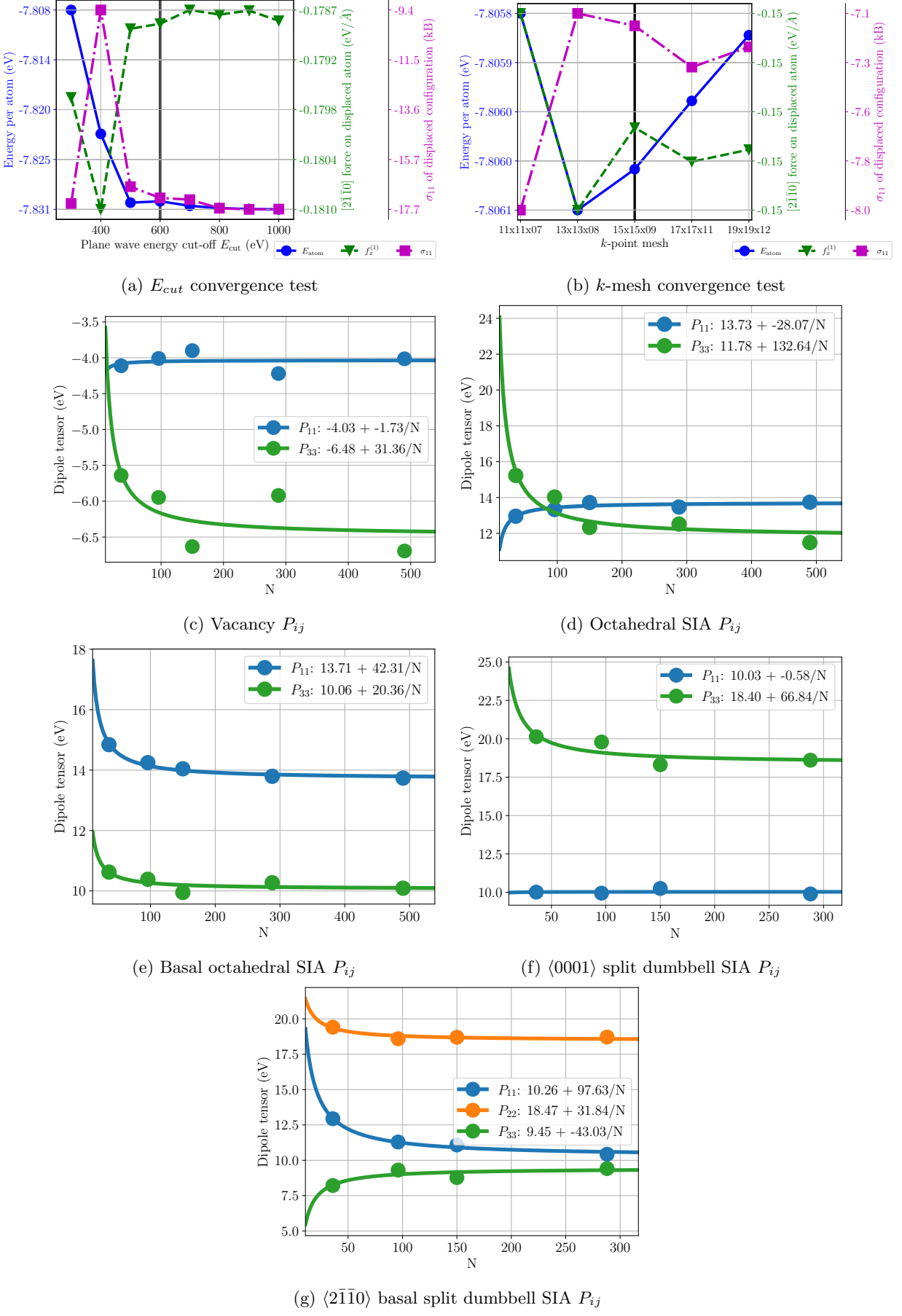


FIG. 25: Titanium

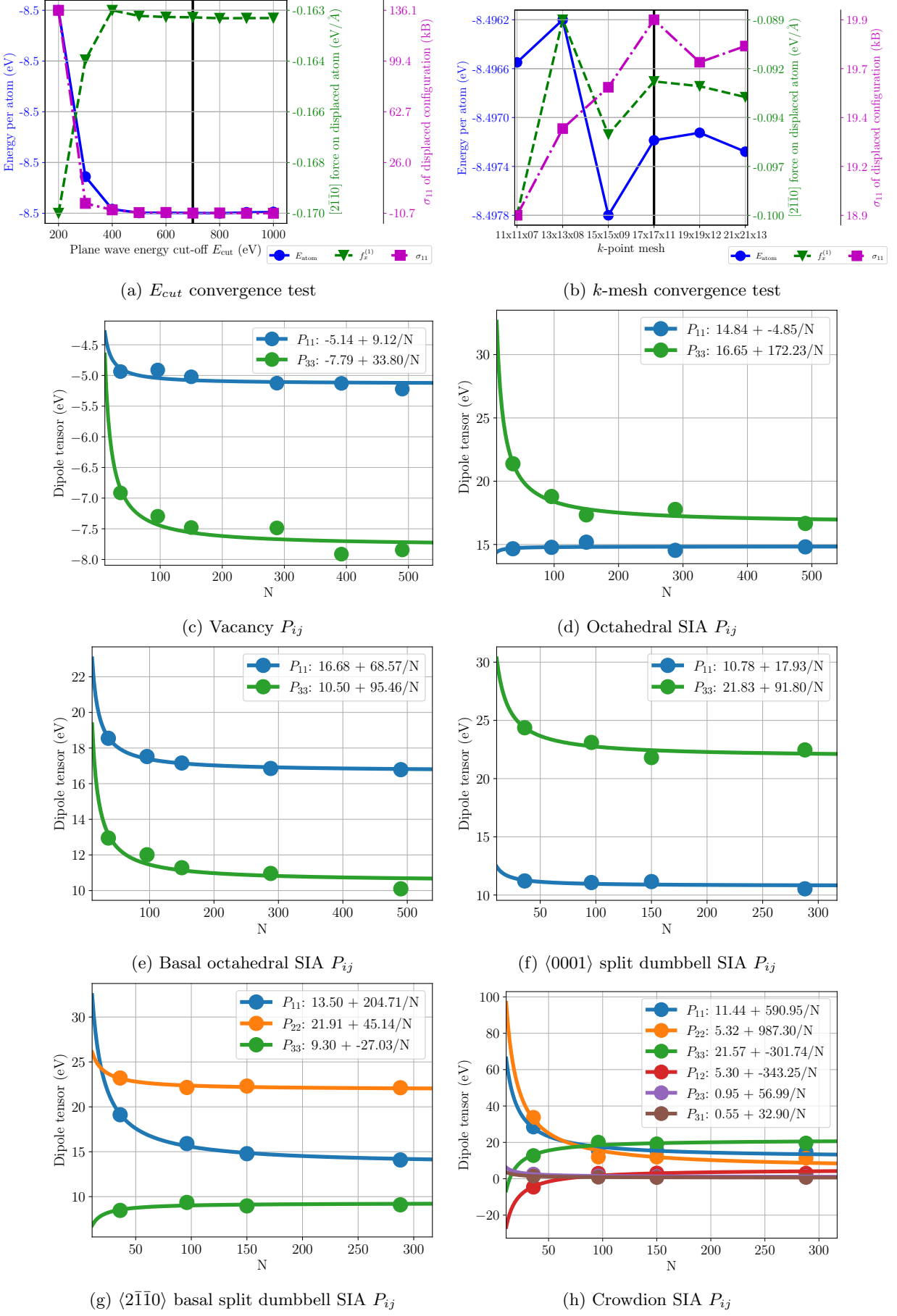


FIG. 26: Zirconium

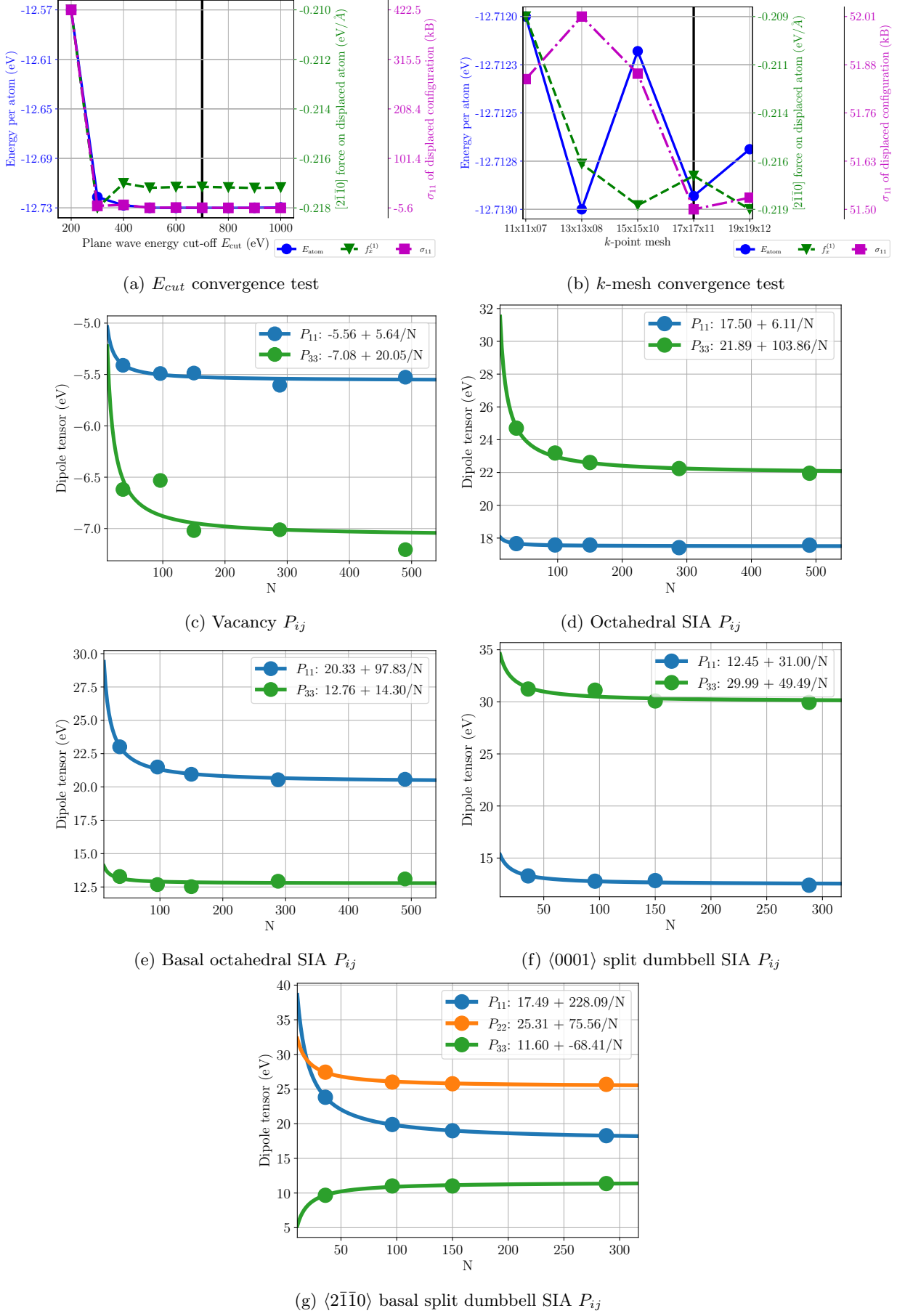


FIG. 27: Hafnium

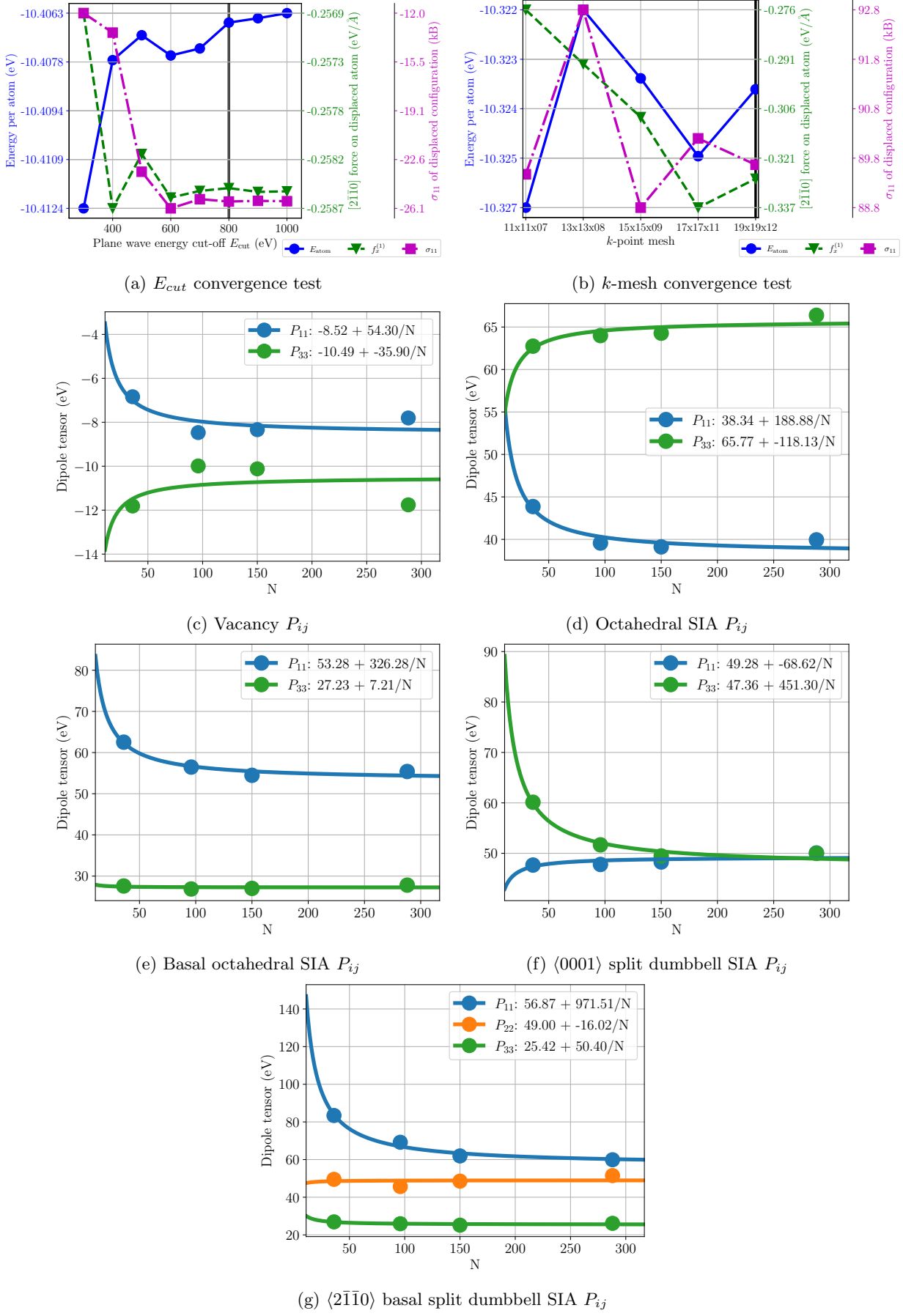


FIG. 28: Technetium

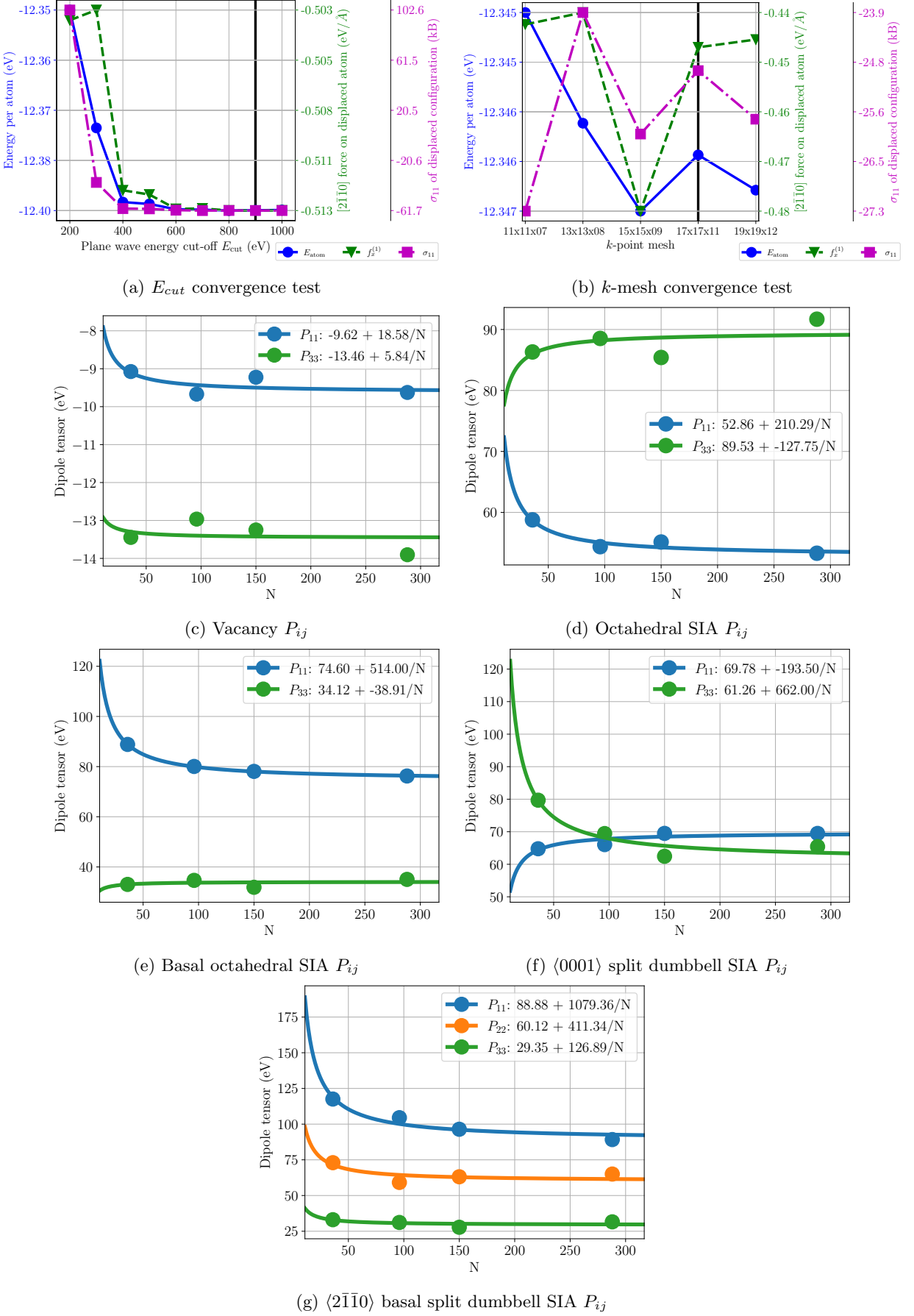


FIG. 29: Rhenium

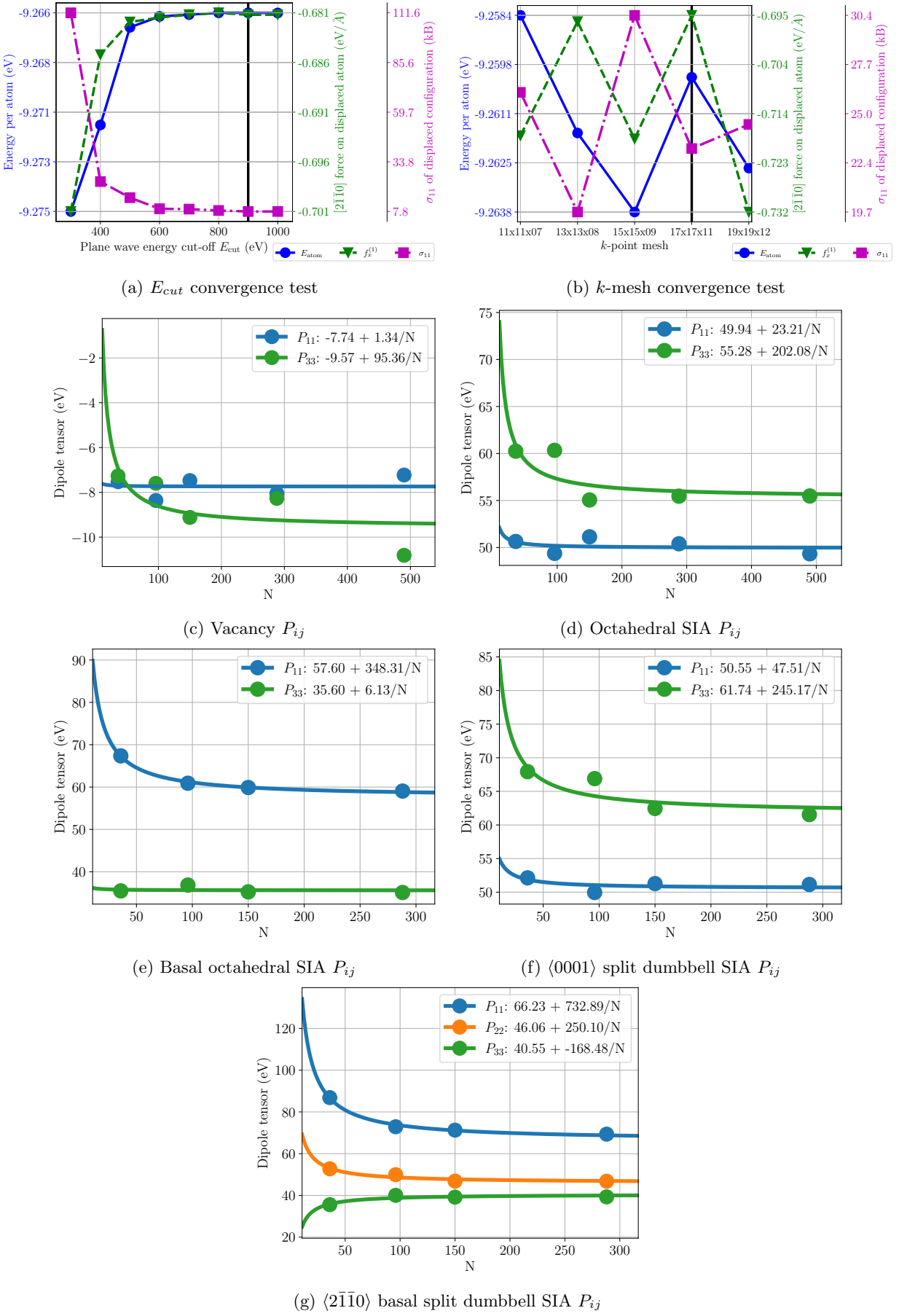


FIG. 30: Ruthenium

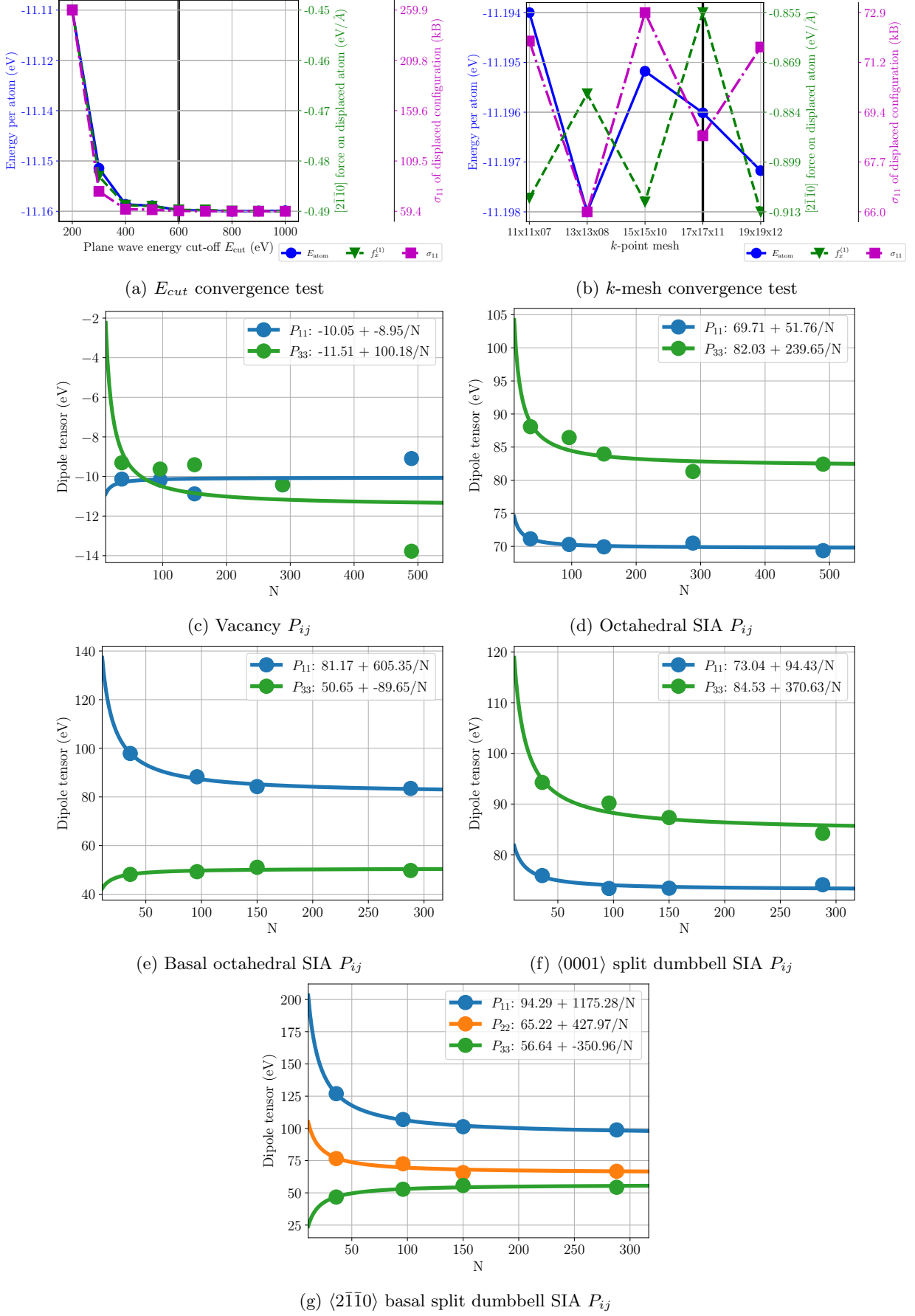


FIG. 31: Osmium

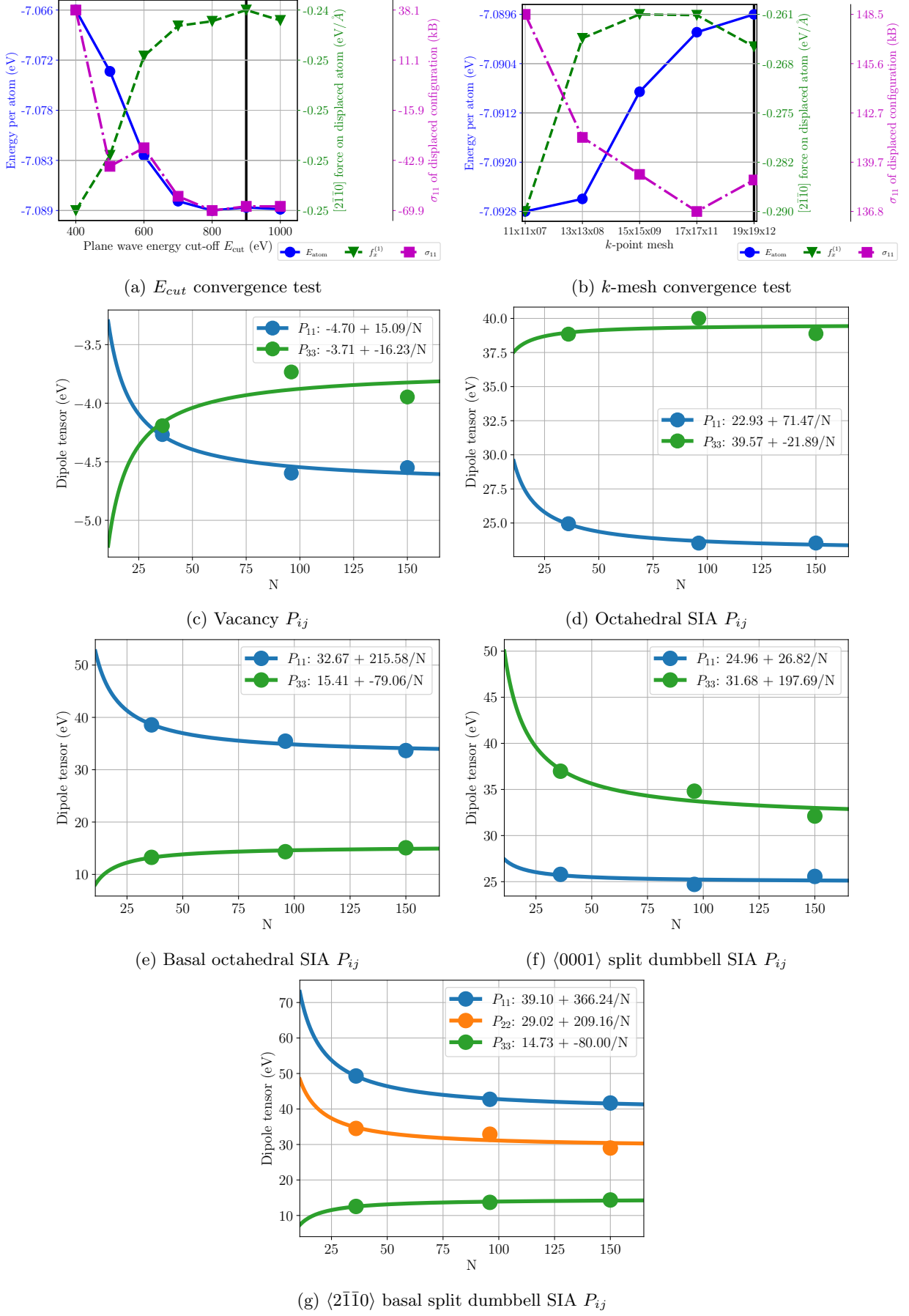


FIG. 32: Cobalt

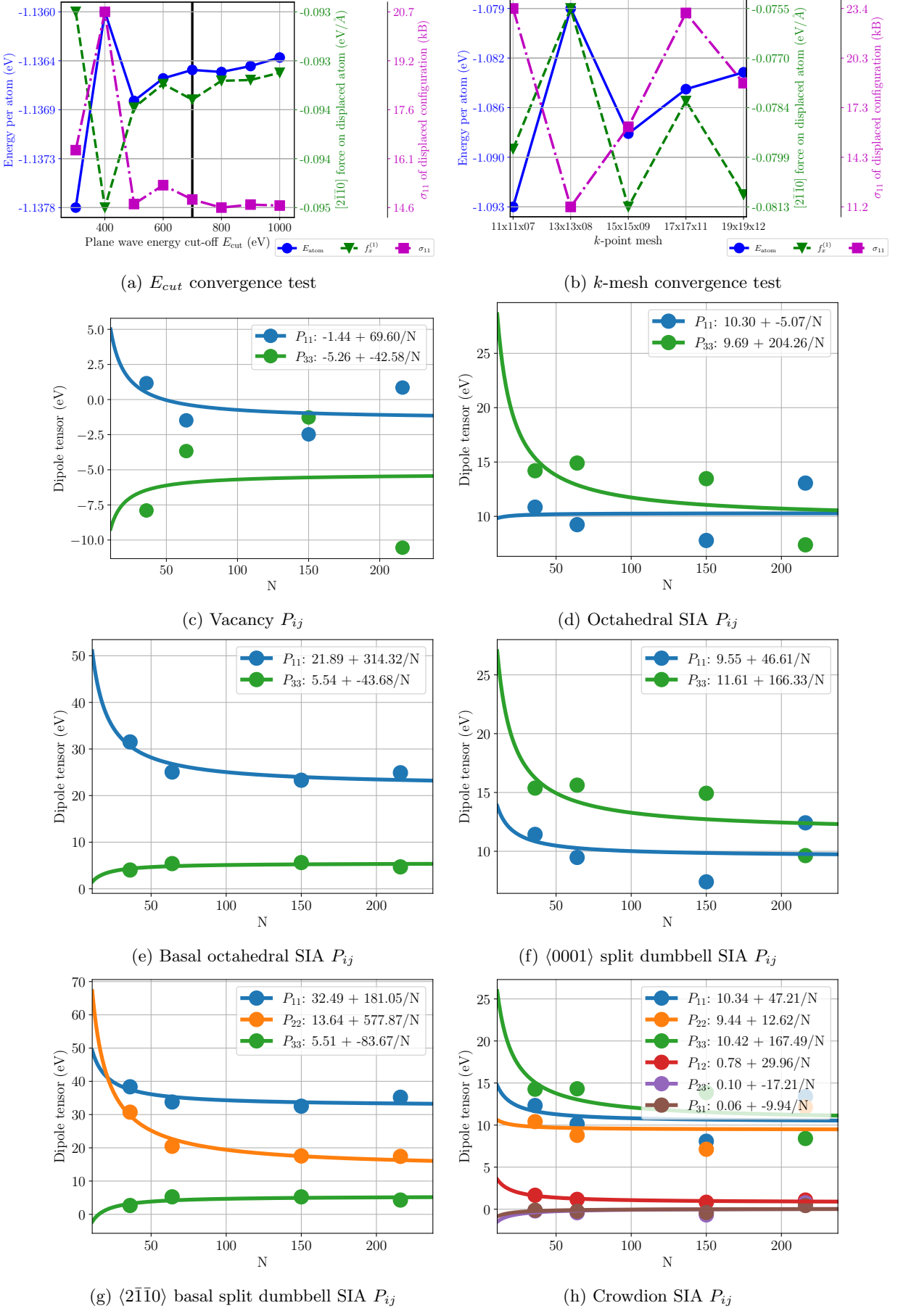


FIG. 33: Zinc

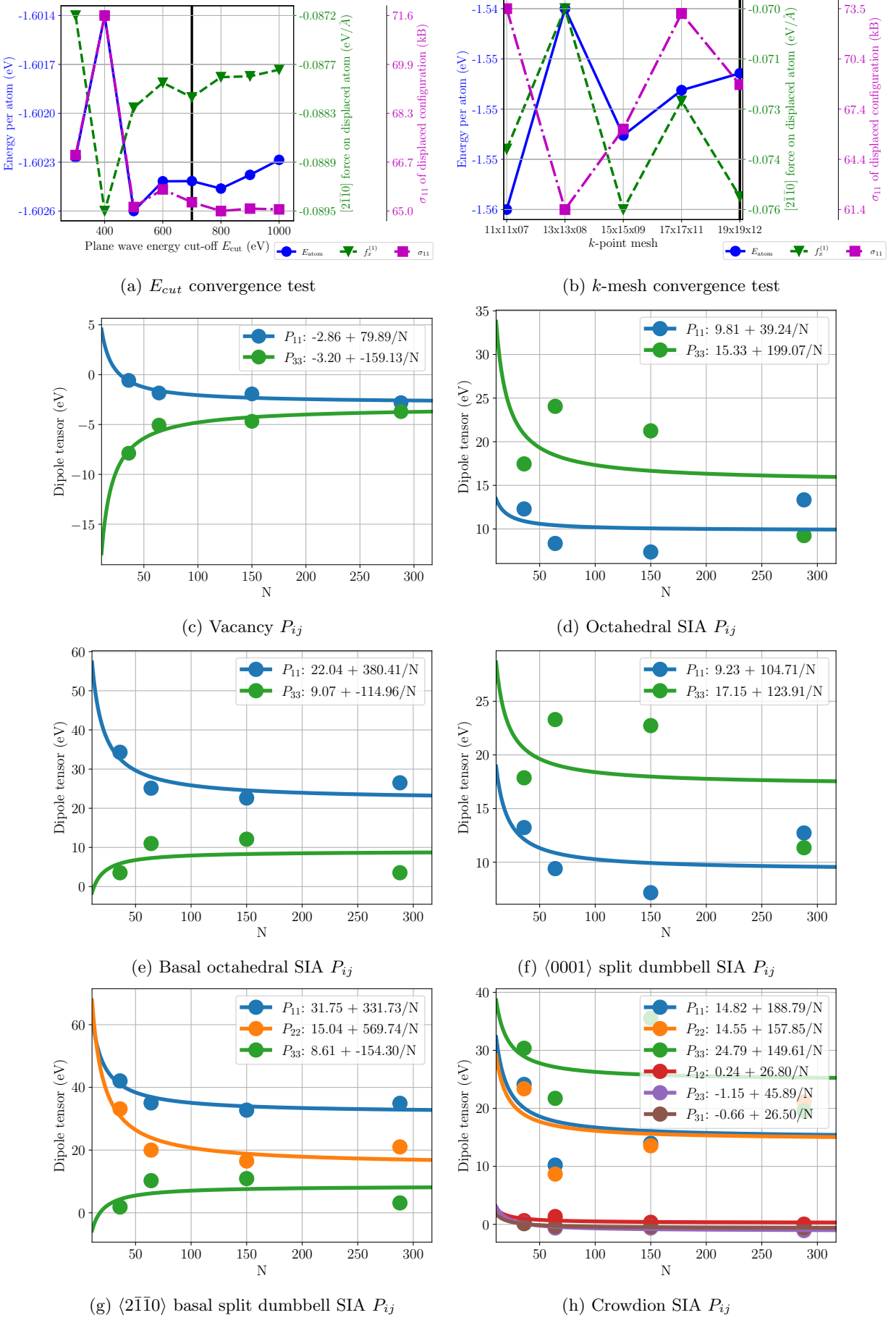


FIG. 34: Zinc PBEsol

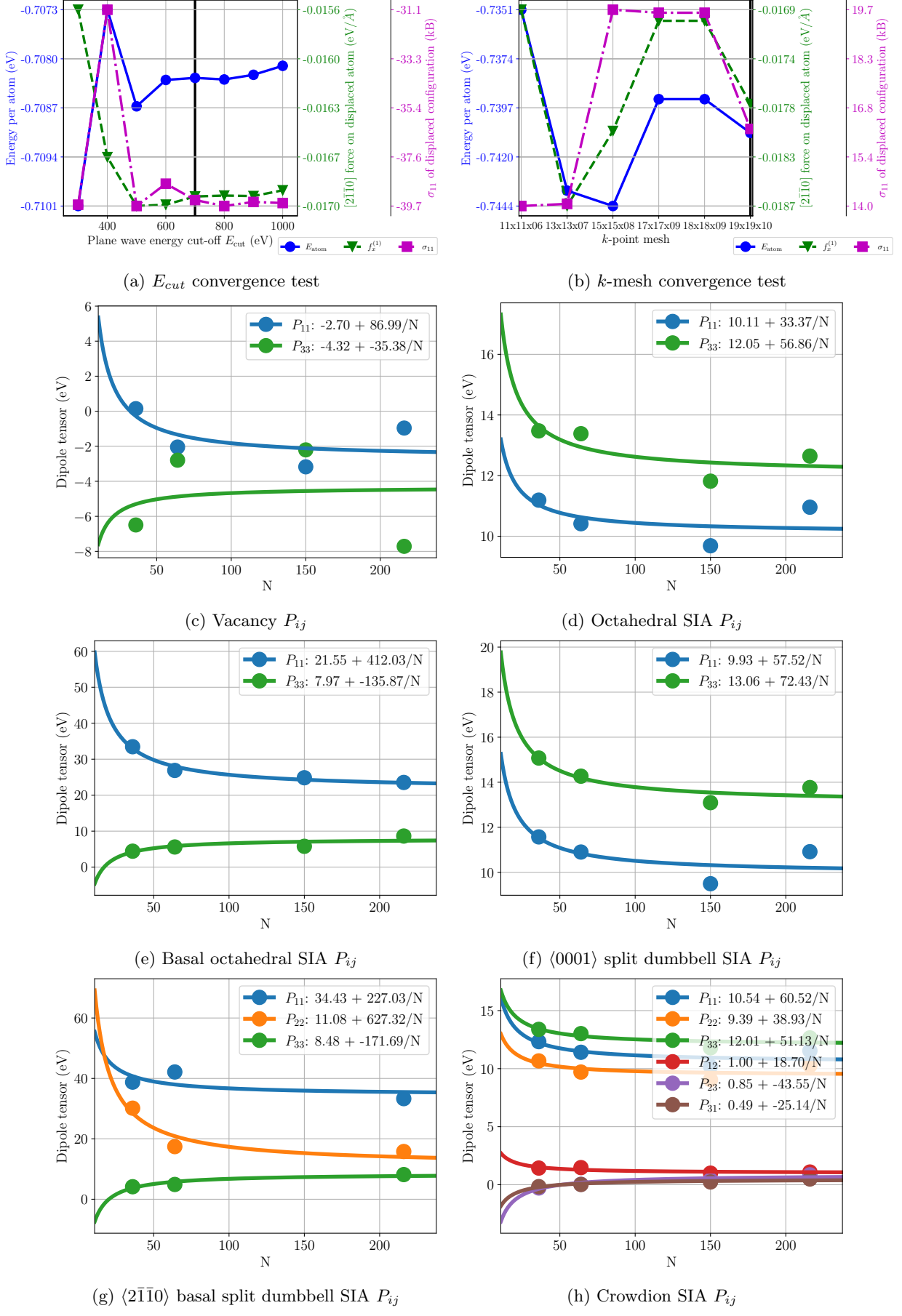


FIG. 35: Cadmium

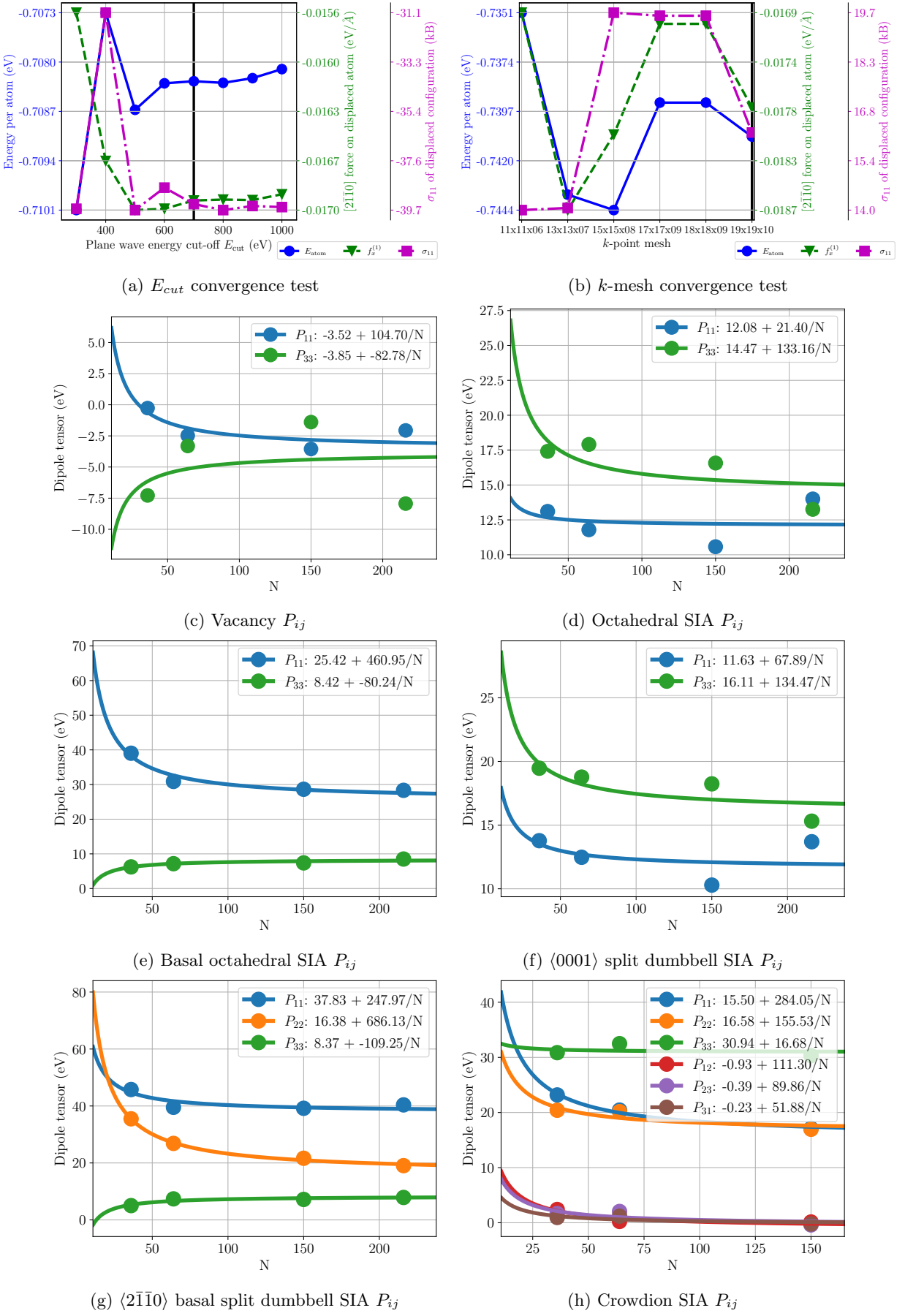


FIG. 36: Cadmium PBEsol

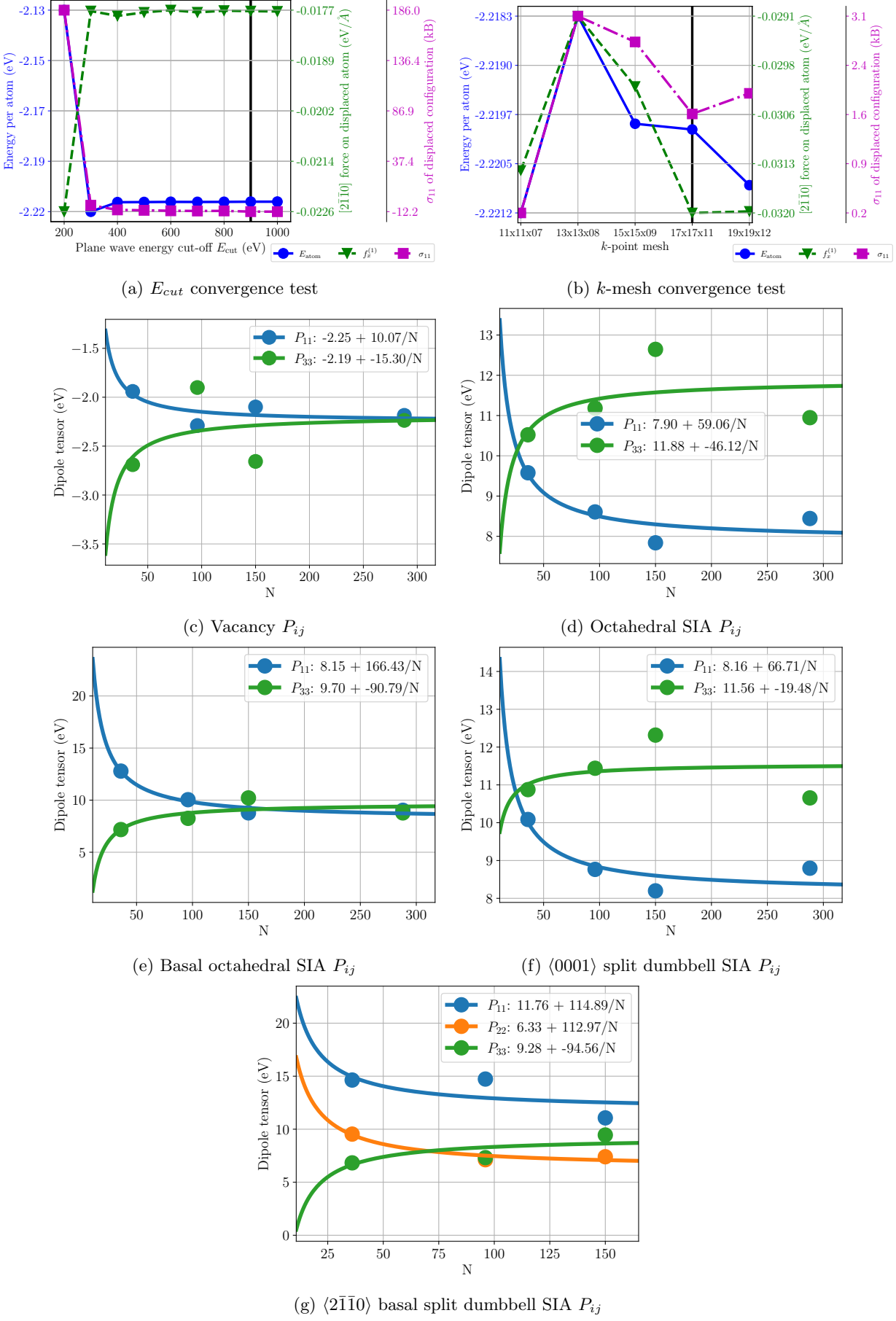


FIG. 37: Thallium

- [1] G. Leibfried and N. Breuer, *Point Defects in Metals I*, Springer Tracts in Modern Physics 81, Vol. 81 (Springer-Verlag, 1978).
- [2] P.-W. Ma and S. L. Dudarev, Universality of point defect structure in body-centered cubic metals, *Physical Review Materials* **3**, 013605 (2019).
- [3] P.-W. Ma and S. L. Dudarev, Nonuniversal structure of point defects in face-centered cubic metals, *Physical Review Materials* **5**, 13601 (2021).
- [4] A. P. Sutton, *Physics of Elasticity and Crystal Defects* (Oxford University Press, 2020).
- [5] D. Nguyen-Manh, A. P. Horsfield, and S. L. Dudarev, Self-interstitial atom defects in bcc transition metals: Group-specific trends, *Physical Review B* **73**, 020101 (2006).
- [6] P. Olsson, *Ab initio* study of interstitial migration in fe-cr alloys, *Journal of Nuclear Materials Fusion Reactor Materials*, **386-388**, 86 (2009).
- [7] P.-W. Ma and S. L. Dudarev, Symmetry-broken self-interstitial defects in chromium, molybdenum, and tungsten, *Physical Review Materials* **3**, 043606 (2019).
- [8] S. V. S. Prasad, S. B. Prasad, K. Verma, R. K. Mishra, V. Kumar, and S. Singh, The role and significance of magnesium in modern day research-a review, *Journal of Magnesium and Alloys* **10**, 1 (2022).
- [9] J. C. Williams and R. R. Boyer, Opportunities and issues in the application of titanium alloys for aerospace components, *Metals* **10**, 705 (2020).
- [10] R. B. Adamson, C. E. Coleman, and M. Griffiths, Irradiation creep and growth of zirconium alloys: A critical review, *Journal of Nuclear Materials* **521**, 167 (2019).
- [11] T. Wang, P. Liu, S. Wang, S. Wang, X. Yi, W. Han, Q. Zhan, and F. Wan, A review on irradiated beryllium and beryllium alloy for fusion reactor application: Microstructure evolution, properties changes, and fabrication, *Fusion Engineering and Design* **211**, 114780 (2025).
- [12] R. C. Pasianot, Self-interstitials structure in the hcp metals: A further perspective from first-principles calculations, *Journal of Nuclear Materials* **481**, 147 (2016).
- [13] G. Vérité, C. Domain, C.-C. Fu, P. Gasca, A. Legris, and F. Willaime, Self-interstitial defects in hexagonal close packed metals revisited: Evidence for low-symmetry configurations in Ti, Zr, and Hf, *Physical Review B* **87**, 134108 (2013).
- [14] D. J. Oh and R. A. Johnson, Relationship between ca ratio and point defect properties in HCP metals, *Journal of Nuclear Materials* **169**, 5 (1989).
- [15] A. M. Monti, Dipole Tensors and Volume Changes of Point Defects in H.C.P. Lattices, *physica status solidi (b)* **168**, 49 (1991).
- [16] W. Hu, H. Deng, X. Yuan, and M. Fukumoto, Point-defect properties in HCP rare earth metals with analytic modified embedded atom potentials, *The European Physical Journal B - Condensed Matter* **34**, 429 (2003).
- [17] T. Angsten, T. Mayeshiba, H. Wu, and D. Morgan, Elemental vacancy diffusion database from high-throughput first-principles calculations for fcc and hcp structures, *New Journal of Physics* **16**, 015018 (2014).
- [18] S.-L. Shang, B.-C. Zhou, W. Y. Wang, A. J. Ross, X. L. Liu, Y.-J. Hu, H.-Z. Fang, Y. Wang, and Z.-K. Liu, A comprehensive first-principles study of pure elements: Vacancy formation and migration energies and self-diffusion coefficients, *Acta Materialia* **109**, 128 (2016).
- [19] M. S. Nitol, D. E. Dickel, and C. D. Barrett, Artificial neural network potential for pure zinc, *Computational Materials Science* **188**, 110207 (2021).
- [20] M. Ganchenkova, P. Vladimirov, and V. Borodin, Vacancies, interstitials and gas atoms in beryllium, *Journal of Nuclear Materials* **386-388**, 79 (2009).
- [21] L. Ferry, F. Virot, Y. Ferro, D. Matveev, C. Linsmeier, and M. Barrachin, Diffusivity of hydrogen and properties of point defects in beryllium investigated by DFT, *Journal of Nuclear Materials* **524**, 323 (2019).
- [22] V. A. Borodin and P. V. Vladimirov, Vacancies and interstitials in yttrium, *Journal of Physics: Condensed Matter* **31**, 185401 (2019).
- [23] S. J. Wooding, D. J. Bacon, and W. J. Phythian, A computer simulation study of displacement cascades in α -titanium, *Philosophical Magazine A* **72**, 1261 (1995).
- [24] M. Wen, C. H. Woo, and H. Huang, Atomistic studies of stress effects on self-interstitial diffusion in α -titanium, *Journal of Computer-Aided Materials Design* **7**, 97 (2000).
- [25] A. Tunde Raji, S. Scandolo, R. Mazzarello, S. Nseniyumva, M. Härtig, and D. Thomas Britton, Ab initio pseudopotential study of vacancies and self-interstitials in hcp titanium, *Philosophical Magazine* **89**, 1629 (2009).
- [26] S. K. Nayak, C. J. Hung, V. Sharma, S. P. Alpay, A. M. Dongare, W. J. Brindley, and R. J. Hebert, Insight into point defects and impurities in titanium from first principles, *npj Computational Materials* **4**, 11 (2018).
- [27] C. K. Ong, Vacancies in α -Zirconium, *physica status solidi (b)* **112**, 312 (1982).
- [28] N. de Diego, Y. N. Ossetsky, and D. J. Bacon, Mobility of interstitial clusters in alpha-zirconium, *Metallurgical and Materials Transactions A* **33**, 783 (2002).
- [29] C. Domain and A. Legris, Ab initio atomic-scale determination of point-defect structure in hcp zirconium, *Philosophical Magazine* **85**, 569 (2005), ISBN: 2331334625.
- [30] N. de Diego, Y. Ossetsky, and D. Bacon, Structure and properties of vacancy and interstitial clusters in α -zirconium, *Journal of Nuclear Materials* **374**, 87 (2008).
- [31] N. de Diego, A. Serra, D. J. Bacon, and Y. N. Ossetsky, On the structure and mobility of point defect clusters in alpha-zirconium: a comparison for two interatomic potential models, *Modelling and Simulation in Materials Science and Engineering* **19**, 035003 (2011).
- [32] G. Samolyuk, S. Golubov, Y. Ossetsky, and R. Stoller, Self-interstitial configurations in hcp Zr: a first principles analysis, *Philosophical Magazine Letters* **93**, 93 (2013).
- [33] Q. Peng, W. Ji, H. Huang, and S. De, Stability of self-interstitial atoms in hcp-Zr, *Journal of Nuclear Materials* **429**, 233 (2012).
- [34] Q. Peng, W. Ji, H. Huang, and S. De, Axial ratio dependence of the stability of self-interstitials in HCP structures, *Journal of Nuclear Materials* **437**, 293 (2013).
- [35] M. Christensen, W. Wolf, C. Freeman, E. Wimmer, R. Adamson, L. Hallstadius, P. Cantonwine, and E. Mader, Diffusion of point defects, nucleation of dislocation loops, and effect of hydrogen in hcp-Zr: Ab initio and classical simulations, *Journal of Nuclear Materials*

- 460**, 82 (2015).
- [36] G. Samolyuk, A. Barashev, S. Golubov, Y. Osetsky, and R. Stoller, Analysis of the anisotropy of point defect diffusion in hcp Zr, *Acta Materialia* **78**, 173 (2014).
- [37] Q. Peng, W. Ji, J. Lian, X.-J. Chen, H. Huang, F. Gao, and S. De, Pressure effect on stabilities of self-Interstitials in HCP-Zirconium, *Scientific Reports* **4**, 5735 (2015).
- [38] C. Varvenne and E. Clouet, Elastic dipoles of point defects from atomistic simulations, *Physical Review B* **96**, 224103 (2017).
- [39] A. J. Fendrik, A. M. Monti, and E. J. Savino, Self-Interstitial in Hexagonal Close-Packed Metals, *physica status solidi (b)* **113**, 709 (1982).
- [40] X. Li, Y. Qin, J. Fu, and J. Zhao, A Gupta potential for magnesium in hcp phase, *Computational Materials Science* **98**, 328 (2015).
- [41] K. Fan, J. Tang, Q. Sun, S. Wu, and X. Wang, First-principles Study on the Properties of Point Defects in Hcp-Dy, in *Proceedings of the International Conference on Advances in Energy, Environment and Chemical Engineering* (Atlantis Press, Paris, France, 2015).
- [42] K. Fan, L. Yang, S. M. Peng, X. G. Long, Z. Wu, and X. T. Zu, Analytical Interatomic Potential for HCP-Scandium, *Materials Science Forum* **689**, 39 (2011).
- [43] D. J. Bacon, Point defects and clusters in the hcp metals: their role in the dose transition, *Journal of Nuclear Materials* **206**, 249 (1993).
- [44] Arblaster, John W., *Selected Values of the Crystallographic Properties of the Elements* (ASM International, United States of America, 2018) ISBN: 9781627081542.
- [45] G. Kresse and J. Hafner, *Ab initio* molecular dynamics for liquid metals, *Physical Review B* **47**, 558 (1993).
- [46] G. Kresse and J. Hafner, *Ab initio* molecular-dynamics simulation of the liquid-metal–amorphous-semiconductor transition in germanium, *Physical Review B* **49**, 14251 (1994).
- [47] G. Kresse and J. Furthmüller, Efficiency of *ab initio* total energy calculations for metals and semiconductors using a plane-wave basis set, *Computational Materials Science* **6**, 15 (1996).
- [48] G. Kresse and J. Furthmüller, Efficient iterative schemes for *ab initio* total-energy calculations using a plane-wave basis set, *Physical Review B* **54**, 11169 (1996).
- [49] G. Kresse and J. Hafner, Norm-conserving and ultrasoft pseudopotentials for first-row and transition elements, *Journal of Physics: Condensed Matter* **6**, 8245 (1994).
- [50] G. Kresse and D. Joubert, From ultrasoft pseudopotentials to the projector augmented-wave method, *Physical Review B* **59**, 1758 (1999).
- [51] J. P. Perdew, K. Burke, and M. Ernzerhof, Generalized Gradient Approximation Made Simple, *Physical Review Letters* **77**, 3865 (1996).
- [52] J. P. Perdew, A. Ruzsinszky, G. I. Csonka, O. A. Vydrov, G. E. Scuseria, L. A. Constantin, X. Zhou, and K. Burke, Restoring the Density-Gradient Expansion for Exchange in Solids and Surfaces, *Physical Review Letters* **100**, 136406 (2008).
- [53] Simmons, Gene and Wang, Herbert, *Single Crystal Elastic Constants and Calculated Aggregate Properties*, 2nd ed. (The MIT Press, 1971) ISBN: 9780262190923.
- [54] J. J. Tonnies, K. A. Gschneidner, Jr., and F. H. Spedding, Elastic Moduli and Thermal Expansion of Lutetium Single Crystals from 4.2 to 300°K, *Journal of Applied Physics* **42**, 3275 (1971).
- [55] C. Pantea, I. Stroe, H. Ledbetter, J. B. Betts, Y. Zhao, L. L. Daemen, H. Cynn, and A. Migliori, Elastic constants of osmium between 5 and 300 K, *Physical Review B* **80**, 024112 (2009).
- [56] R. G. Leisure, R. B. Schwarz, A. Migliori, and M. Lei, Room-temperature elastic constants of Sc and ScD_{0.18}, *Physical Review B* **48**, 1276 (1993).
- [57] A. F. Guillermet and G. Grimvall, Thermodynamic properties of technetium, *Journal of the Less Common Metals* **147**, 195 (1989).
- [58] Y. Le Page and P. Saxe, Symmetry-general least-squares extraction of elastic data for strained materials from *ab initio* calculations of stress, *Physical Review B* **65**, 104104 (2002).
- [59] X. Wu, D. Vanderbilt, and D. R. Hamann, Systematic treatment of displacements, strains, and electric fields in density-functional perturbation theory, *Physical Review B* **72**, 035105 (2005).
- [60] H. P. Myers and W. Sucksmith, The spontaneous magnetization of cobalt, *Proceedings of the Royal Society of London. Series A. Mathematical and Physical Sciences* **207**, 427 (1977).
- [61] S. L. Dudarev and P.-W. Ma, Elastic fields, dipole tensors, and interaction between self-interstitial atom defects in bcc transition metals, *Physical Review Materials* **2**, 033602 (2018).
- [62] P.-W. Ma and S. Dudarev, CALANIE: Anisotropic elastic correction to the total energy, to mitigate the effect of periodic boundary conditions, *Computer Physics Communications* **252**, 107130 (2020).
- [63] M. I. Aroyo, ed., *International Tables for Crystallography: Space-group symmetry*, 2nd ed., Vol. A (International Union of Crystallography, 2016).
- [64] C. Varvenne, F. Bruneval, M.-C. Marinica, and E. Clouet, Point defect modeling in materials: Coupling *ab initio* and elasticity approaches, *Physical Review B* **88**, 134102 (2013).
- [65] E. Clouet, S. Garruchet, H. Nguyen, M. Perez, and C. S. Becquart, Dislocation interaction with C in α -Fe: A comparison between atomic simulations and elasticity theory, *Acta Materialia* **56**, 3450 (2008).
- [66] H. Ullmaier, ed., *Atomic Defects in Metals*, Vol. 25 (Springer-Verlag, Berlin/Heidelberg, 1991) series Title: Landolt-Börnstein - Group III Condensed Matter Publication Title: Atomic Defects in Metals.
- [67] N. Gaston, D. Andrae, B. Paulus, U. Wedig, and M. Jansen, Understanding the hcp anisotropy in cd and zn: the role of electron correlation in determining the potential energy surface, *Physical Chemistry Chemical Physics* **12**, 681 (2009).
- [68] P. Ehrhart and B. Schönfeld, Investigation of electron-irradiated zinc by diffuse X-ray scattering. I. Self-interstitials in zinc, *Physical Review B* **19**, 3896 (1979).
- [69] D. R. Mason, D. Nguyen-Manh, M.-C. Marinica, R. Alexander, A. E. Sand, and S. L. Dudarev, Relaxation volumes of microscopic and mesoscopic irradiation-induced defects in tungsten, *Journal of Applied Physics* **129**, 075112 (2019).
- [70] L. Reali, M. Boleininger, M. R. Gilbert, and S. L. Dudarev, Macroscopic elastic stress and strain produced by irradiation, *Nuclear Fusion* **62**, 016002 (2022).